Stockholm University

Bachelor Thesis

Degree Project in
Geology 15 hp

Glaucophane pseudomorphs in high pressure metapelites: a petrogenic investigation

Gregor Weltz

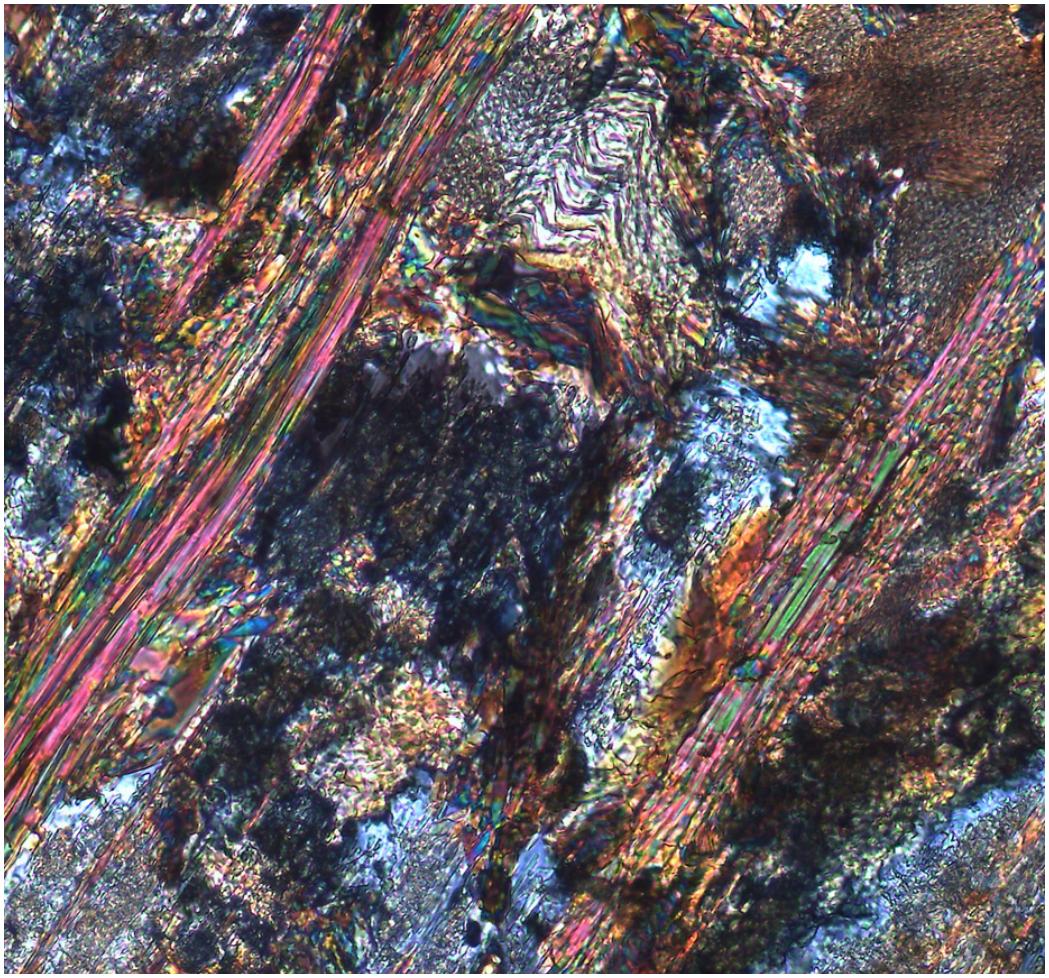

Stockholm 2024

Department of Geological Sciences
Stockholm University
SE-106 91 Stockholm

Abstract

This thesis investigates the glaucophane pseudomorphs in high-pressure metapelites from the Muret Unit in the northern Dora-Maira Massif, Western Alps. Through a detailed petrographic analysis of two thin sections of garnet micaschist, this study tries to gain a deeper insight into the P-T path followed by the Muret Unit during exhumation, by identifying the minerals produced by glaucophane consumption. Glaucophane pseudomorphs display complex textures and contain a range of fine-grained minerals suggesting that different glaucophane breakdown reactions took place at micrometre scale. More generally, this study aims to test the viability of using glaucophane pseudomorph products to understand a possible heating stage during late exhumation, a process invoked in the Alps and linked to slab break-off.

Contents

1. Introduction

Glaucophane is a sodic amphibole indicative of the blueschist metamorphic facies and thus ultimately linked to subduction zones (Bucher, 2005). It can occur in both, metapelites and metabasites (Coleman, 1967) and is, therefore, not rare by any means. Furthermore, as glaucophane contains water, it can provide an excellent record of conditions during retrogression as it easily metamorphoses itself (Jenkins and Juan Corona, 2006).

The Dora-Maira Massif in the Western Alps is a natural laboratory to investigate glaucophane breakdown reactions. Recent studies (Campomenosi et al., 2021, Minghardi et al., 2023) in this Massif suggest a late stage of heating at low pressure (~ 0.5 GPa) before further cooling. This event has been linked to slab break-off. Slab break-off is the process during which a more buoyant piece of lithosphere detaches from the tectonic plate during subduction. This, in turn, leads to the heating of the overriding lithosphere as it allows for hotter, asthenospheric mantle material to flow upward (von Blanckenburg and Davies, 1995).

Figure 1 represents two end-members pressure-temperature (P-T) paths that may be followed by tectonometamorphic units during exhumation. The minerals produced by glaucophane breakdown may help to define the T conditions attained during exhumation and thus are a key to unraveling potential late heating stage.

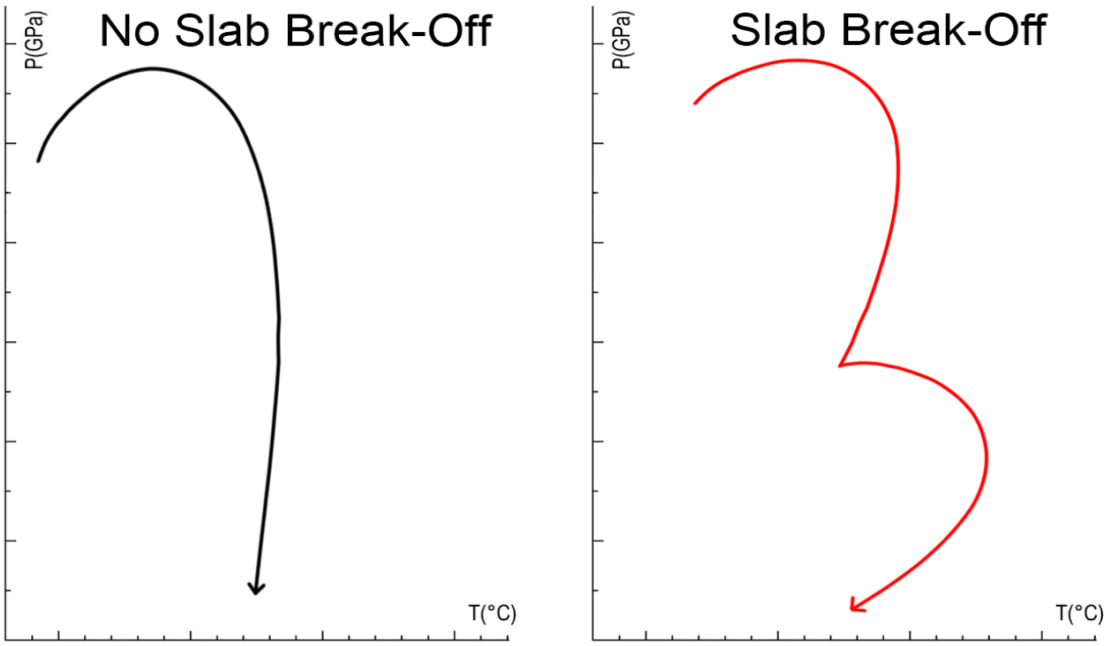

Figure 1: Two potential P-T paths followed by tectonometamorphic units during the formation of a mountain belt.

This study investigates a garnet-glaucophane micaschist from the Muret Unit in the northern Dora-Maira Massif. In this thesis, cm-sized glaucophane pseudomorphs are studied to identify glaucophane breakdown reactions and their mineral products. These data are used to evaluate a potential heating stage at low P during late exhumation.

2. Geological setting

The Dora-Maira Massif in the Western Alps was part of the Briançonnais microcontinent which bordered the Piemonte-Liguria Ocean (Bonnet et al., 2022), a part of the Tethys Ocean (Le Breton et al., 2021). The present architecture of the Western Alps results from the Variscan and Alpine orogenic cycles (e.g. Nosenzo et al. 2022). During the Alpine cycle, the Piemonte-Liguria Ocean was subducted, and the European and Adriatic plates collided (Le Breton et al., 2021).

The Dora-Maira Massif consists of various tectonometamorphic units (see Table 1). In the south, these units are (from top to bottom) the Sanfront-Pierolo Unit, San Chiaffredo Unit, Brossasco-Isasca Unit, Rocca-Solei Unit, Ricordone Unit and Dronero-Sampeyre Unit. The Sanfront-Pinerolo is the lower-most unit of this nappes stack (Bonnet et. al., 2022). This area has been largely investigated since the discovery of coesite in the Brossasco-Isasca Unit (Chopin 1984).

In the northern Dora-Maira Massif (see Figure 2), from top to bottom, the units are the Pinerolo Unit, Chasteiran Unit, Muret Unit, Serre Unit. This area remains more poorly explored (Nosenzo et al., 2024).

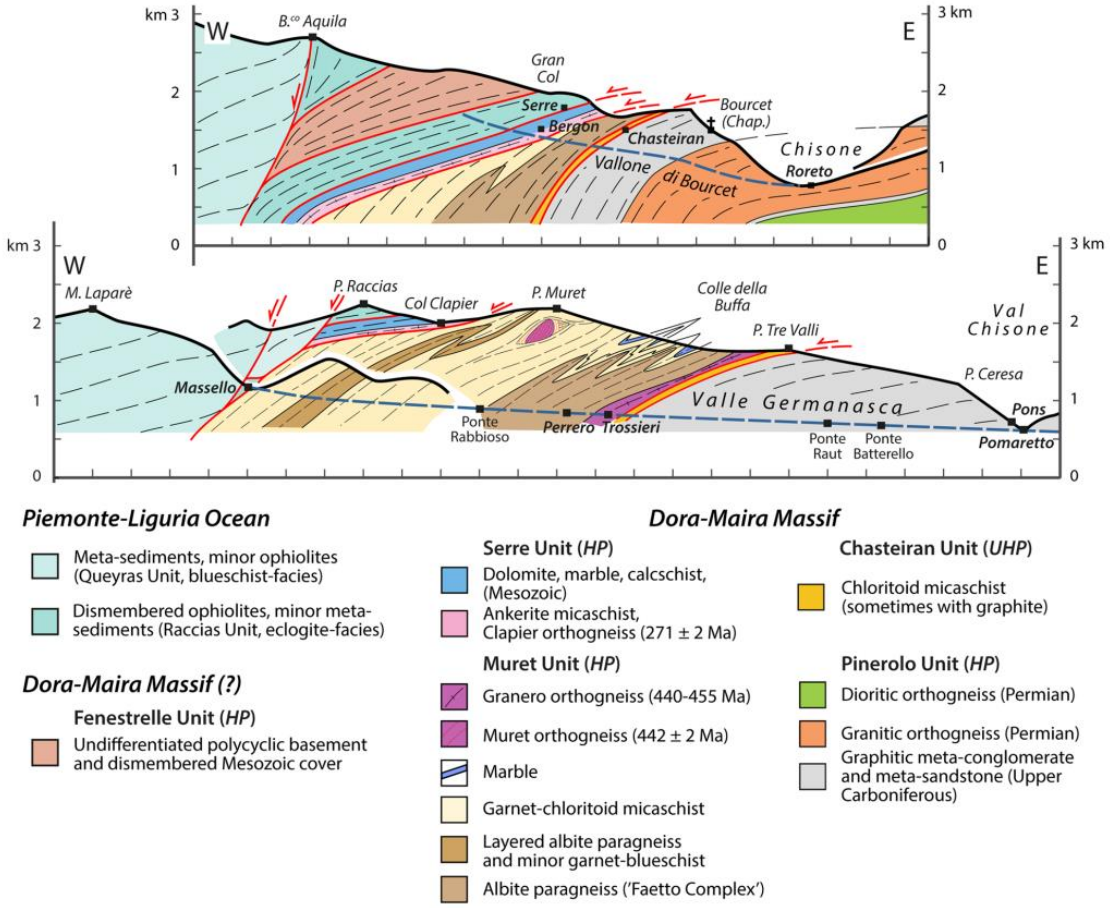

Figure 2: Cross-sections in the Northern Dora-Maira Massif (Nosenzo et al., 2024).

Sector	Unit	Lithologies	Alpine P-T conditions
North + South	Sanfront-Pinerolo	- Blueschist-greenschist, orthogneiss, quartzite layers (D. Avigad, Chopin and R. Le Bayon, 2003)	20–24 kbar and 500–515°C (Groppo et al., 2019) 14–16 kbar 400–500°C (Avigad et al., 2003)
South	San Chiaffredo	- UHP quartz-eclogite (Groppo et al., 2019) - "cold" eclogite facies (Bonnet et al., 2022)	Peak: 20–24 kbar and 500–520°C (Groppo et al., 2019)
South	Brossasco-Isasca	- Garnet bearing white schists with coesite inclusions in garnet, orthogneiss, metapelite, eclogite and marble (Groppo et al., 2019)	Peak: 30–35 kbar, 675–720°C Retrograde: 5 kbar and 575–600°C (ibid.)
South	Rocca-Solei	- Augen gneiss, garnet-bearing blue amphibole- metabasite (Balestro et al., 2020)	Peak: around 22 kbar and 510°C (Groppo et al., 2019)
South	Ricordone	- garnet-chloritoid mica schist, garnet mica schist (Bonnet et al., 2022)	433 -475°C (ibid.)
South	Dronero-Sampeyre	- garnet-chloritoid schists, orthogneiss and metabasites (André Michard et al., 2022)	Peak: 17-18 kbar and 450-470°C (Groppo et al., 2019)
North	Chasteiran	- chloritoid micaschist with thin graphite layers, coesite-bearing garnets (Manzotti et al., 2022)	27–28 kbar and 510–530°C (ibid.)
North	Muret	- orthogneiss, garnet-staurolite micaschist, garnet micaschist (Nosenzo et al., 2022)	High strain: 18–19 kbar 480–510 ◦C Low strain: 21–22 kbar 530–560 ◦C (Nosenzo, Manzotti and Robyr, 2023)
North	Serre	- Felsic gneiss, orthogneiss, micaschist, marbles, calcschist (Nosenzo et al., 2024)	To be determined

Table 1: Main lithologies and P-T estimates for the various units of the Dora-Maira Massif.

The northern part of the Dora-Maira is less explored compared to the southern part. As an example, the Chasteiran Unit has only recently been discovered by Manzotti et al. (2022) and for the Serre Unit, Nosenzo et. al. (2024) point out that further research is needed to constrain P-T estimates.

The samples investigated in this study were collected in the Muret Unit (44° 58' 10.54'' N, 7° 06' 26.38'' E). In the following, the main characters (lithologies and Alpine metamorphic conditions) of the Muret Unit are briefly described. The main lithologies in the Muret Unit are garnet-chloritoid micaschist, paragneiss, and minor calcite-rich marbles (Nosenzo et al., 2024). Largely homogenous paragneisses vary in thickness from 10 m to 1 km. They contain few garnets and, because of the lack of chloritoid, are believed to have formed from greywackes. On a smaller scale, some paragneisses contain albite, epidote, and blue and green amphiboles.

The Muret Unit is generally strongly deformed by the Alpine deformation, but a few low-strain domains have been recognised (e.g., Nosenzo et al., 2022). An example is the low-strain domain of the Punta Muret, which is only a few km in size are comprised of orthogneiss and garnet-staurolite micaschist.

Overall, garnet-chloritoid micaschist are quite widespread in the Muret Unit. They show alternating quartz and mica bands with chloritoid in the mica domains. Polycyclic garnet crystals are quite common and comprise a pre-Alpine and Alpine garnet generation. Pre-Alpine garnet crystals are larger (1-3mm) than Alpine garnets (<0.3mm). Polycyclic garnet-chloritoid micaschist have been investigated for determining the P-T conditions of the pre-Alpine and Alpine metamorphism of the Muret Unit (Nosenzo et al., 2022, Nosenzo, Manzotti and Robyr, 2023). According to these studies, the Muret Unit reached P-T conditions of 6-8 kbar and 640–660°C during the pre-Alpine (Variscan) cycle and P-T conditions of 21-22 kbar and up to 550 °C during the Alpine cycle.

Locally, micaschist in the Muret Unit displays only one garnet generation with garnet crystals up to 1cm in size (Nosenzo et al., 2024). The structural and metamorphic history of this micaschist has not been investigated in detail so far and represents the core of this thesis.

3. Methods

3.1 Thin section analyses

Thin sections were scanned using a Nikon Coolscan 9000, in cross-polarised light (XPL) and plane-polarised light (PPL). Mineral distribution was estimated by image analysis of the scanned thin sections. Five main minerals can be clearly identified from the images: white mica, quartz, garnet, pseudomorphed glaucophane and minor amounts of ilmenite. The images were loaded in Photoshop and the respective minerals were overpainted with an individual colour. For ilmenite, the colour selection tool was used to mark all black pixels on the PPL images, yielding very accurate results. Finally, using the histogram, the total amount of pixels of each colour was counted and a percentage of each mineral could be derived: white mica (42%), quartz (36%), pseudomorphed glaucophane (18%), garnet (6%), and ilmenite (0.1%). The pseudomorphed glaucophane itself, consists of roughly equal parts albite, biotite, chlorite and green amphibole. Because of their small crystal size and intergrowth, they cannot be estimated with this method. The method used can be compared to point counting.

The microscopy work was performed with a Leica DMLSP microscope and microphotographs were taken with a Leica MC170 HD at full resolution. Calibration was carried out manually according to the specifications of the camera and double-checked with a calibrated measure. Then, both thin sections were analysed thoroughly, and microphotographs of important observations were taken. If necessary, white balance and exposure levels were adjusted in image post-processing.

On several occasions (Figure 23, 24 or 36-38) panoramic stitches were built. This serves the purpose that one can create a large-scale image, for example of a large crystal, while retaining high resolution. For example, Figure 24, shows a glaucophane 5 mm across. Here, using the 10x zoom lens on the microscope, 44 single pictures with 30% overlap were taken. Then, these were stitched together to form an 80-megapixel image retaining beautiful detail while also allowing for a general overview of the entire crystal. The full-resolution image is provided digitally.

3.2 Mineral chemistry

The chemical compositions of several minerals (e.g., garnet, muscovite, chloritoid, and chlorite) were recalculated based on their structural formulae. In this study, values are reported as a.p.f.u. unless specified otherwise. The data was acquired at the electron microprobe in Brest (France) by the lab manager, Jessica Langlade. Minerals were classified following the classification of Deer, Howie and Zussman (2013). Since none of the samples contain significant amounts of Mn (>0.01), it is sufficient to calculate X_{Mg} as $1- X_{Mg} = X_{Fe}$.

3.3 Garnet-chloritoid thermometry

Temperature was calculated using the garnet-chloritoid thermometer of Perchuk (1991) where:

$$T\ in\ °C = \frac{2150.5}{(ln_{Kd}+1.773)} - 273.15$$

and

$$K_d = (\frac{X_{Mg}}{1-X_{Mg}})^{ctd} * (\frac{1-X_{Mg}}{X_{Mg}})^{grt}$$

4. Petrography

The two thin sections cut from the garnet micaschist (sample GM1923a and GM1923b) are very similar for mineralogical content and deformation history and are, therefore, described together below.

White Mica

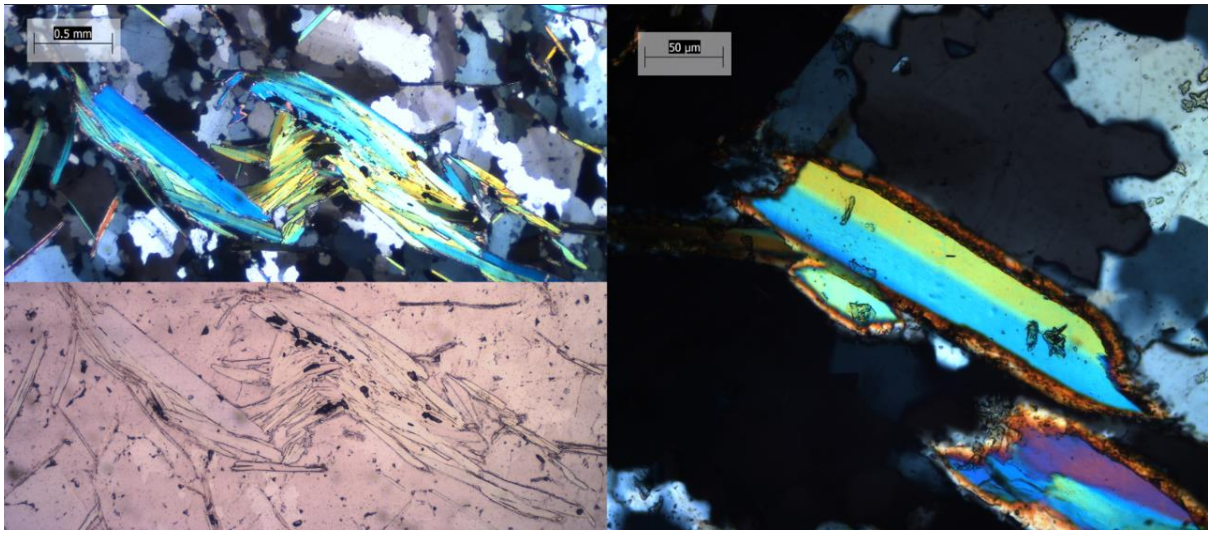

Figure 3: Examples of white mica in sample 1923a (PPL and XPL photomicrographs). On the left side, crenulation of the mica crystals can be observed. Similar microstructures are rather common in the samples. On the right side, a mica corona is visible. These are less common at roughly 5% of crystals.

In PPL, white mica is colourless with moderate relief. Under XPL, 2nd order red, blue, and yellow interference colours can be observed. White mica is anisotropic. Roughly 5% of the crystals in the sample show pronounced coronas. Perfect cleavage (001) is visible in many crystals independent of foliation or crystal orientation. White mica can be found as small inclusions (a few microns in size) in garnet or in the matrix around 1 mm long.

White mica in the matrix defines the main foliation. This foliation is crenulated during stage II (i.e. the folding stage, see section 5 for a detailed description of the deformation history of the studied sample).

Quartz

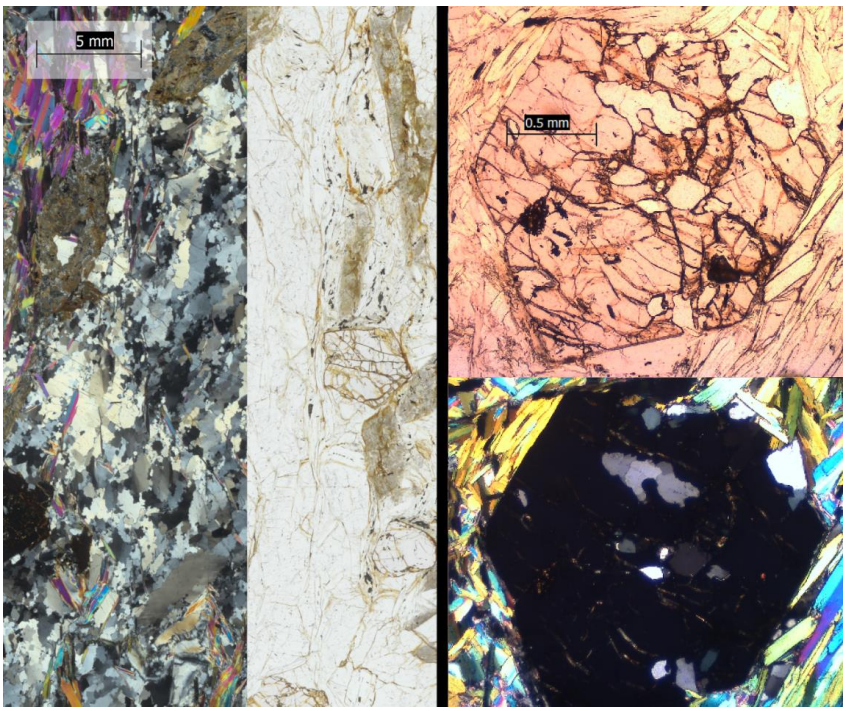

Figure 4: On the left, an XPL and PPL microphotographs of a large Quartz domain. This specific domain is semi-continuous and stretched across roughly 20% of sample 1923a. On the right, a quartz inclusion *in garnet. Quartz is found as inclusions fully enclosed by garnet core and rim.*

Quartz is the second-most common mineral in the two investigated thin sections. It occurs both in large domains and as inclusions in garnet and pseudomorphed glaucophane. In PPL, it is colourless with low relief. It does not show pleochroism or cleavage. In XPL, it exhibits undulose extinction and 1st order white interference colour. Crystal size varies from only a few micrometres for crystals included in garnet, to millimetres in the large domains marking the main foliation S1 (stage I; see section 5) in the matrix.

Pseudomorphed Glaucophane

One of the most striking characteristics of the investigated sample is the occurrence of large pseudomorphed glaucophane crystals. This mineral is never preserved- and thus, no optical properties such as colour, interference colour, cleavage or relief could be observed. However, the typical rhombohedral habit is commonly well-preserved. These euhedral to subhedral crystals are, by far, the largest in the sample. Many of them can be seen with the naked eye and are several millimetres in diameter, the longest reaching close to 10 mm.

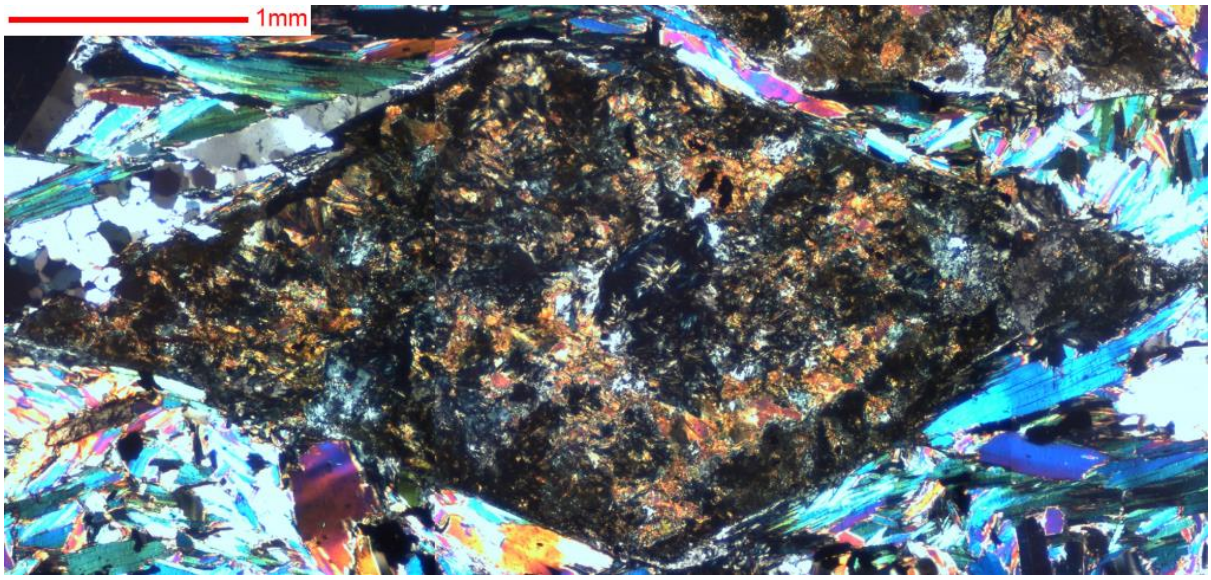

Figure 5: A mm-sized-euhedral glaucophane crystal that has been fully replaced by several minerals. The crystal's orientation is parallel to the main foliation and the sharp tips show no sign of deformation.

Several minerals replaced glaucophane, the most common ones being albite, green amphibole, chlorite, and biotite. In addition, quartz and ilmenite are preserved in smaller amounts. An important observation regarding tectonic stages is that garnet inclusions (from 0.5 to 1 mm in size) have been observed in three pseudomorphs.

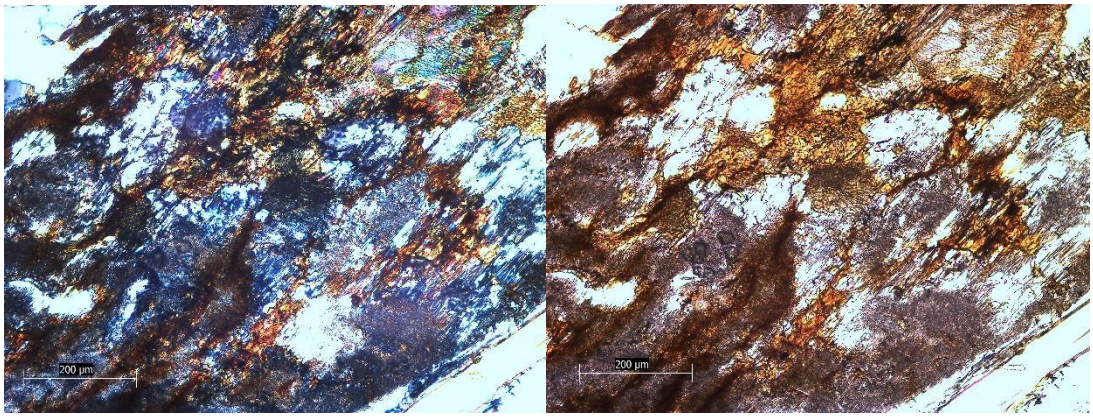

Figure 6: Close-up of minerals that replace glaucophane (XPL left, PPL right). Larger crystals are often albite or chlorite, the groundmass are amphibole, biotite and albite tightly intergrown.

Garnet

Garnets in the sample are mostly subhedral. They have high relief and are isotropic in XPL. They vary strongly in their degree of deformation. While some crystals are barely cracked, others are significantly broken. The cracks of the latter are commonly oxidised which can be seen as brown discolouration in the left image below.

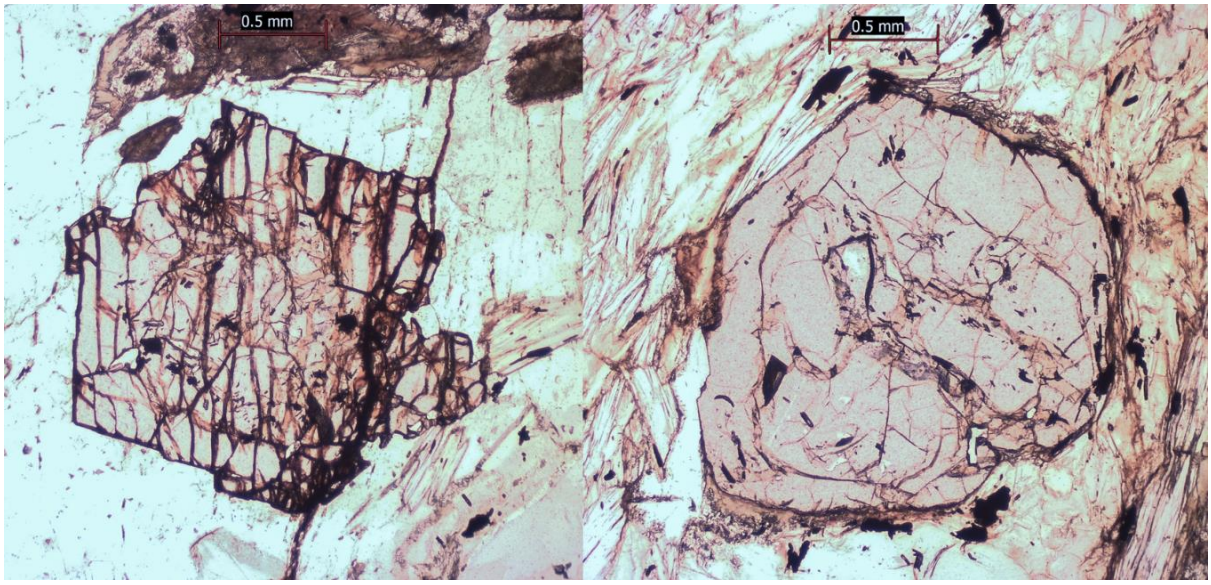

Figure 7: Two examples of mm-sized garnets. The garnet on the left shows a clear direction of preferred cracking which is roughly 45° offset from the main foliation. The garnet on the right shows no clear direction of cracking. Chlorite can be seen on the bottom-left side of the garnet.

Garnets in both samples have several inclusions: quartz, white mica, chloritoid, rutile, and graphite – all of which are described in more detail in their respective sub-section. Apatite occurs as inclusions on the edges or connected to cracks. It needs to be pointed out that no ilmenite is included in garnet, neither in the crystal itself nor connected to cracks. Minerals that appear opaque in PPL turn out to be bundles of rutile when inspected under 40x magnification or larger oxidised areas.

Rutile

Rutile occurs as tiny, tetragonal needle inclusions in garnet. Although it might sometimes appear to be oriented, crystals display several different orientations even within individual garnets. Rutile is dark yellow to brown in PPL and XPL and shows high relief. Interestingly, rutile most often occurs in bundles if the garnet is cracked. In less cracked garnets mainly individual rutile needles are found.

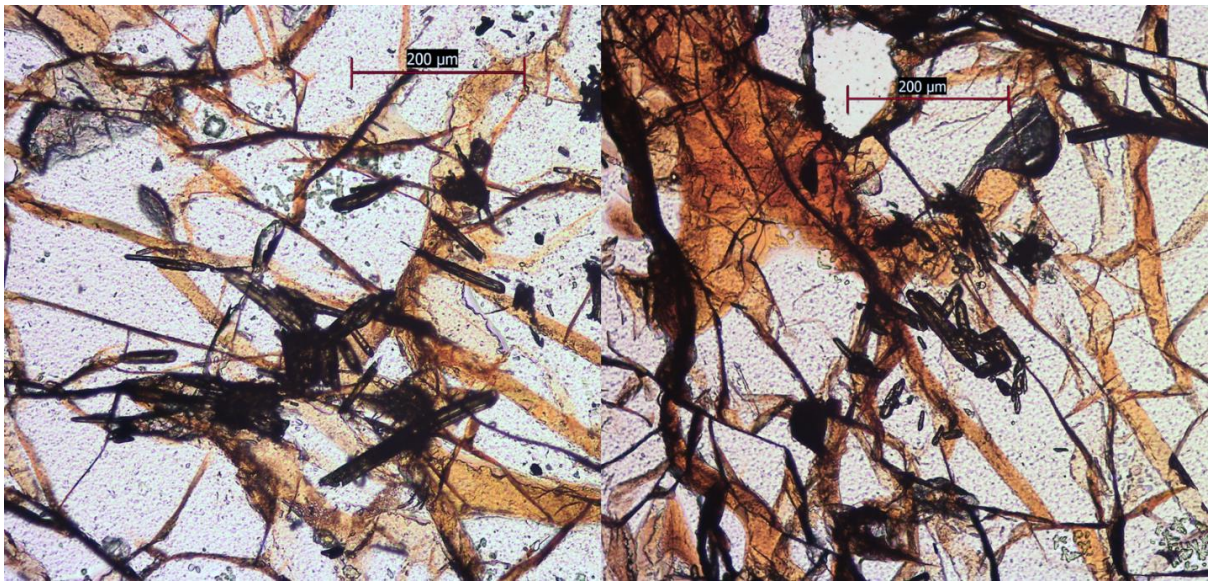

Figure 8: Rutile inclusions in two garnet porphyroblasts (PPL). The orientation of the thin section was not changed to illustrate the different orientations of rutile crystals.

Chloritoid

Small (>100 µm) chloritoid inclusions are found in garnet, generally in groups of several crystals. They are slightly blue or grey in PPL with high relief. Under XPL they show a blueish-white colour. It is important to note that only a few garnet porphyroblasts contain chloritoid inclusions.

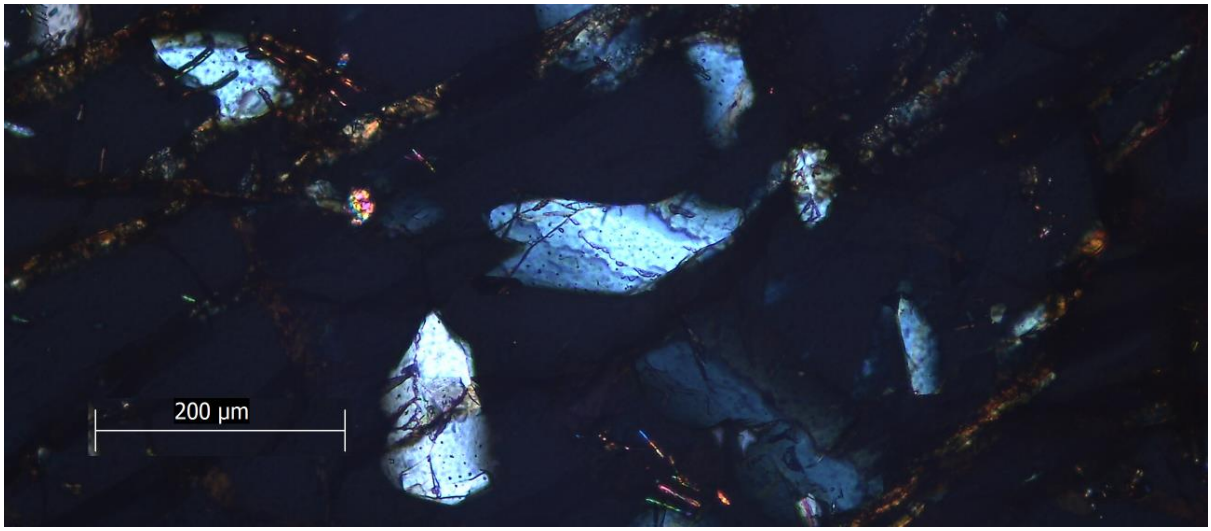

Figure 9: Small chloritoid crystals included in garnet. There is no clear preferred orientation. Chloritoid and quartz can look very similar in the investigated samples. The most distinguishing feature is a subtle blue tint under PPL and the relief.

Apatite

Apatite is found as subhedral prismatic crystals, characterised by high relief and slightly blue colour in PPL while it shows 1st order pale blue interference colour in XPL. Apatite occurs as inclusions in garnet (only located at the rim of the porphyroblasts), but also in the matrix as individual crystals in the muscovite domain. This mineral has not been observed in the pseudomorphed glaucophane.

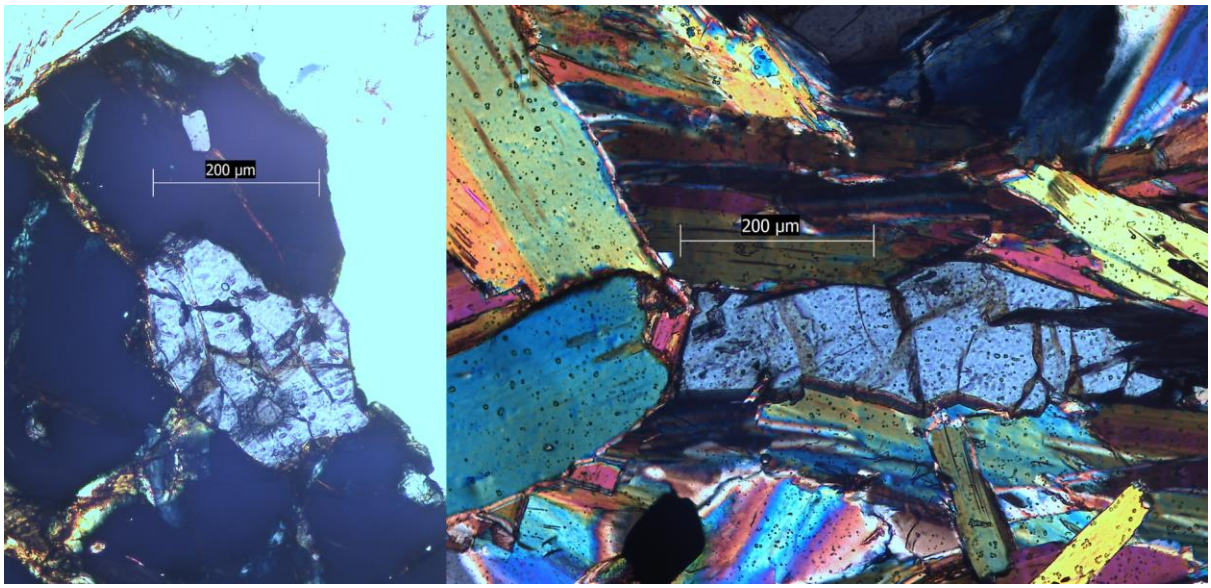

Figure 10: On the left, an apatite in garnet. It is important to note that the crystal in not included in garnet but rather grew connected to the matrix. On the right, an apatite in the matrix, parallel to the main foliation indicated by the surrounding mica.

Green Amphibole

Tiny, green needles can be found replacing the glaucophane in all glaucophane pseudomorphs. In PPL, green amphibole is slightly pleochroic and shows medium relief. In XPL, 2nd order green interference can be observed. Most often, crystals are oriented parallel to the main elongation of the pseudomorphed glaucophane.

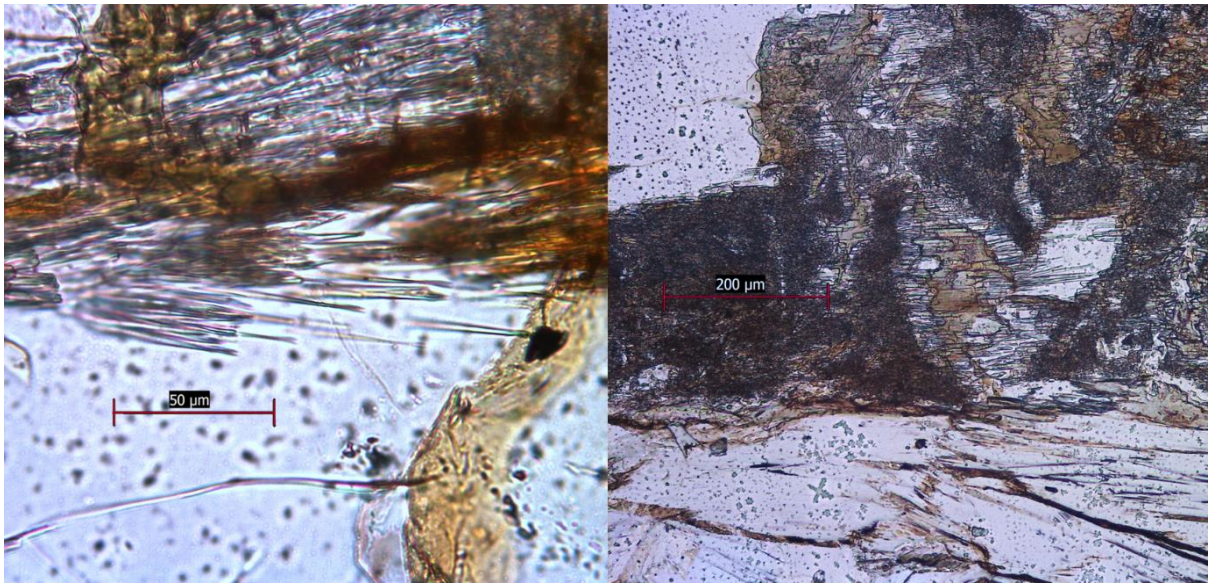

Figure 11: Tiny, micrometre-sized green amphiboles can be seen in pseudomorphed glaucophane. They are almost exclusively oriented parallel to the orientation of the pseudomorphed glaucophane crystal.

Chlorite

As mentioned above, chlorite is one of the main minerals replacing glaucophane. Larger aggregates of chlorite occur at garnet rims, where they can sometimes partially replace garnet. Chlorite exhibits typical green colour and low relief in PPL but a somewhat anomalous pattern with deep blue interference colours under XPL. These typical optical characters of chlorite are better identifiable in the large aggregates replacing garnet than in the tiny crystals replacing glaucophane. However, larger domains of chlorite, making up a significant portion of the replacement products, certainly exist in glaucophane pseudomorphs.

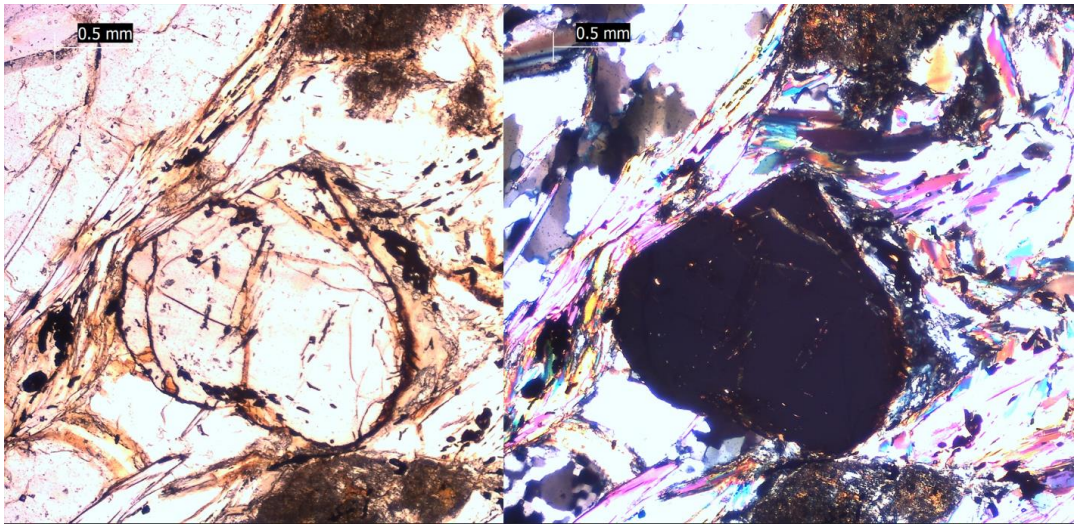

Figure 12: Large aggregate consisting of chlorite can be seen near the rim of the garnet or filling larger garnet cracks. When not associated with glaucophane, chlorite is typical green in PPL. Chlorites in glaucophane are most obvious due to their extinction pattern.

Albite

Albite is only present in the pseudomorphed glaucophane. Sometimes, it is difficult to make a distinction between albite and quartz. Albite, unlike quartz, can show a subtle yellow hue in PPL. The typical extinction patterns such as twinning, or lamellae cannot be observed as the grains are too small and their extinction appears undulose like quartz. The image below shows quartz and albite in XPL. The yellow hue is not visible on camera as it is too subtle. Because of this, some chemical analyses were carried out to gain certainty (Nosenzo 2022, unpublished).

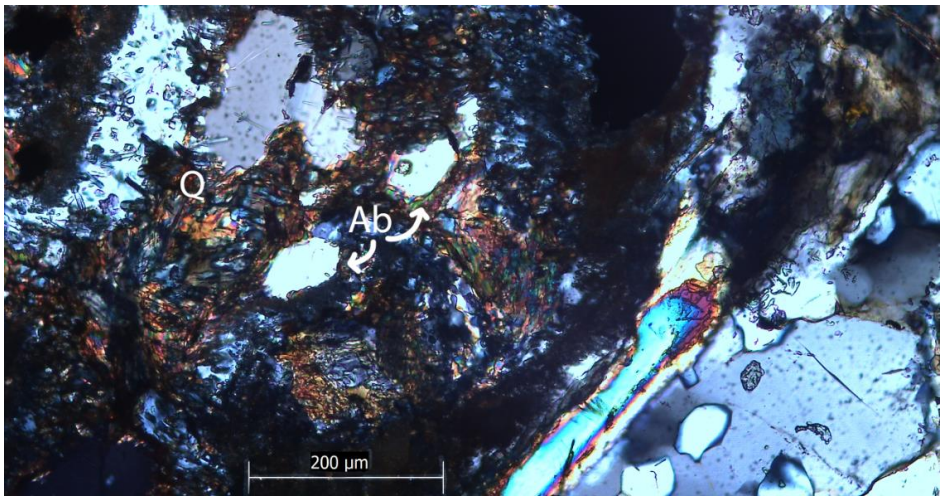

Figure 13: Albite in glaucophane. Crystals range widely in size from several micrometres to several hundreds of micrometres. They can often look like quartz but have a subtle tint under PPL.

Ilmenite

Ilmenite is the only opaque in the sample and thus easily identifiable. It occurs in pseudomorphed glaucophane or in the matrix, frequently associated with white mica. This mineral has not been observed in the quartz domain or in garnet.

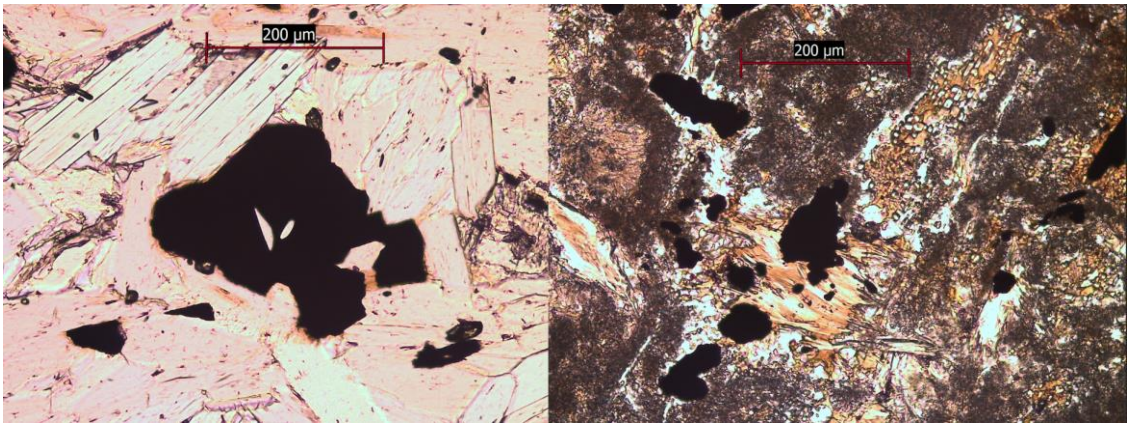

Figure 14: On the left, an ilmenite in the main foliation accompanied by mica. On the right, an inclusion in glaucophane.

Single Crystals

Two, single crystals of tourmaline and epidote were found. The epidote was chemically analysed by (Nosenzo 2022, unpublished). The tourmaline could be identified microscopically. The subhedral, trigonal crystal shape can be recognised. Under PPL it is deep blue and strongly pleochroic with moderate relief. In XPL, it presents the same colour, which is a 2nd order blue. The colour strongly suggests that the tourmaline is an elbaite (Deer, Howie and Zussman, 2013).

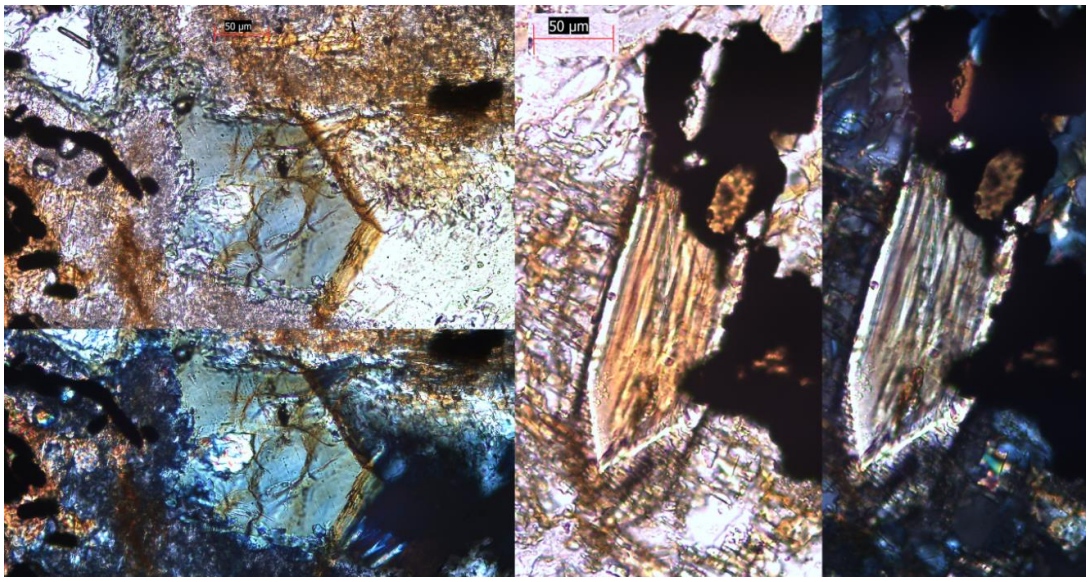

Figure 15: On the left, a beautiful elbaite which shows rich blue colour under PPL. On the right, a sharp epidote crystal. This crystal is the largest recognisable epidote, though chemical analyses suggests that there are several.

5. Structural and metamorphic stages

Based on the microscopic observations, four structural and metamorphic stages can be identified. An overview can be seen in the figure below marking the stable minerals as blue lines.

Mineral	% (est)	Stage 0 (Inclusion in grt)	Stage I (S1 foliation)	Stage II (Folding)	Stage III (Static replacem.)
Quartz (q)	35	—	—	—	—
Muscovite (ms)	41	—	—	—	
Garnet (grt)	5	—	—	—	
Rutile (rt)	<0.1	—	—		
Chloritoid (ctd)	<0.1	—	—	—	—
Graphite (gph)	<0.1	—	—	—	—
Apatite (ap)	<0.1	—	—	—	—
Glaucophane (gln)	17		—	—	
Chlorite (chl)	*30*	—	—	—	—
Ilmenite (ilm)	<0.1				—
Albite (ab)	*30*				—
Green Amphibole (amp)	*30*				—
Biotite (bt)	*10*				—

Figure 16: estimated percentage of minerals, IMA-CNMNC abbreviations (Warr, 2021). Blue lines indicate stability during a stage. Percentages written in italics (chl, ab, amp, bt) are share of said mineral as glaucophane replacement product. These are counted separately as it is important to show the share of what-used-to-be-glaucophane, as well.

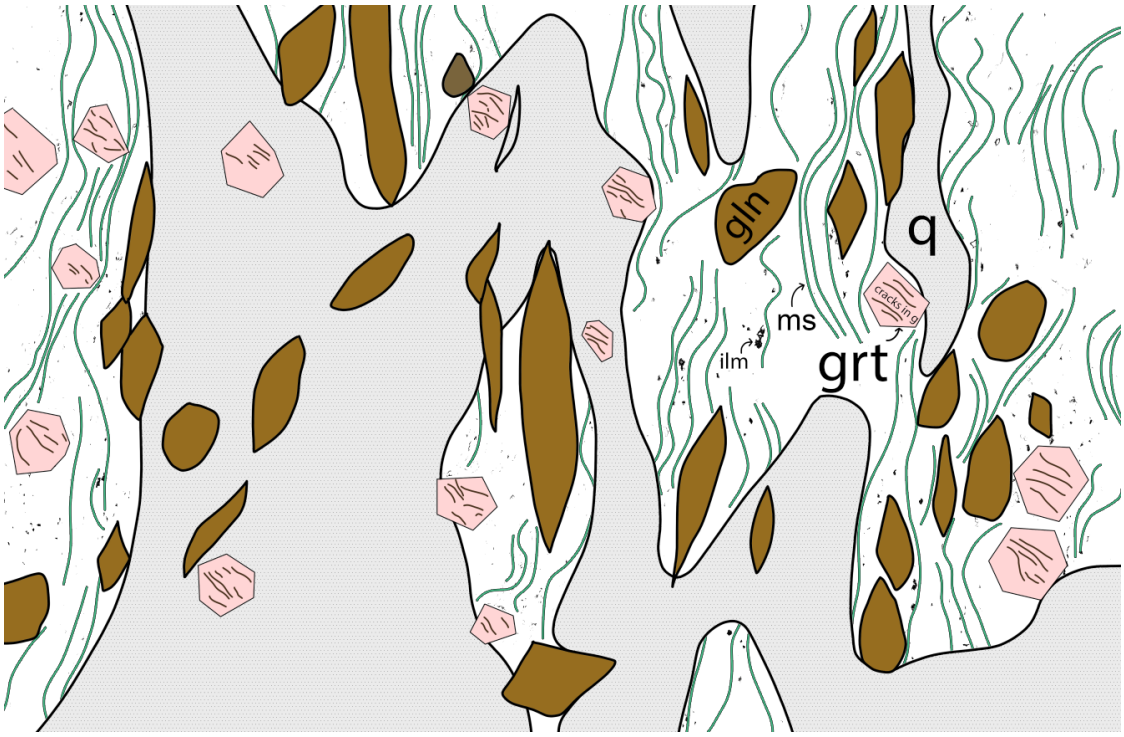

Figure 17: A sketch of thin section GM1923a which displays the clearest foliation. Preferred orientation of garnet-cracks is marked as lines.

Stage 0

This stage is characterised by the minerals that were included in garnet during initial growth. As previously described, those include quartz, chloritoid, apatite, white mica, rutile, and graphite. Interestingly, despite mica being the most abundant mineral in the sample, it is only included in minor amounts. The two most common inclusions are quartz and chloritoid. There is no sign of internal deformation. However, cracks in garnet appear to have a preferred orientation that is believed to have formed at a later stage.

30 10

Stage I

During this stage, the S1 foliation formed as alternating quartz and mica bands. Sample 1923b exhibits a continuous quartz domain through the entire sample with a thickness of around 2-5 mm. The transition from quartz to mica domains is often sharp. It needs to be pointed out, however, that only the mica domains were preserved – not their original S1 crystal orientation. The shape preferred orientation of mica crystals within these domains do not always correspond with the dominant foliation (e.g., stage II).

Stage II – Crenulation and folding

The original S1 foliation was subsequently folded which can be seen in the simplified sketch (see Figure 17). Crenulated mica bands and a continuous, but folded, quartz domain are the most dominant features of this stage. Glaucophane orientation is an important clue of deformation history. The vast majority of glaucophane crystals are oriented parallelly with the foliation that can be observed today. Their orientation is roughly perpendicular to the direction of pressure that crenulated and folded the S1. In quartz bands, there are some smaller glaucophanes that are 45° offset with respect to today's main foliation. Some glaucophanes (n=3) have incorporated smaller garnets. This supports the Stage 0 garnet growth hypothesis as they must have formed before the stability field of glaucophane was entered.

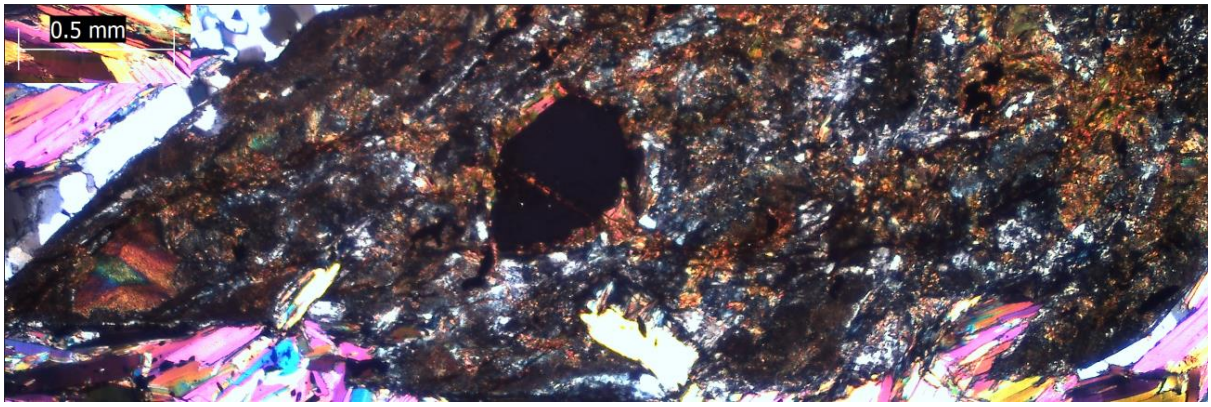

Figure 18: A garnet grain being enclosed by glaucophane.

Almost all mica bands are oriented perpendicular to the direction of stress. This orientation can be caused by either mechanical rotation or oriented growth during prolonged metamorphism. As micas bends easily and only slightly crenulated but no bent micas were found, one can therefore argue that the micas in the sample grew perpendicular to the direction of stress rather than being S1 remnants (Stallard and Shelley, 2005). The fact that glaucophane and mica crystals have the same orientation confirms that glaucophane was stable during stage II and was likely not present during stage I. Apatite, wrapped by mica without visible mica deformation proves the stability of apatite at this stage. A nice example of this can be seen in image below.

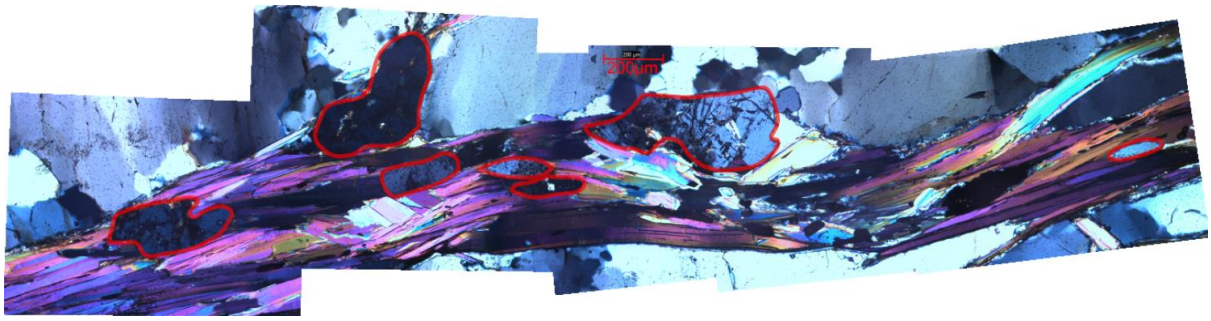

Figure 19: Apatite crystals in the matrix. Extinct apatites are marked red. These mica and apatite crystals are parallel to the main foliation.

Stage III – Static replacement

The final stage that can be observed is dominated by retrograde metamorphism of glaucophane and brittle deformation of garnets. During this stage, minerals which developed during stage II maintain their original orientation but, in case of glaucophane, are completely replaced by chlorite, albite, and green amphibole. The vast majority of green amphibole is oriented parallel to the elongation of the glaucophane. Fractures in garnet often exhibit a preferred orientation. Due to the lack of garnet rotation, this could be seen as a rough record of the strain direction upon release. This is further discussed in section 9.2.

6. Mineral Chemistry

6.1 Garnet

Two garnet chemical profiles were measured. In sample 1923a, the transect consists of 150 points over 2760 micrometres and in sample 1923b the sample contains 109 points over 2300 micrometres.

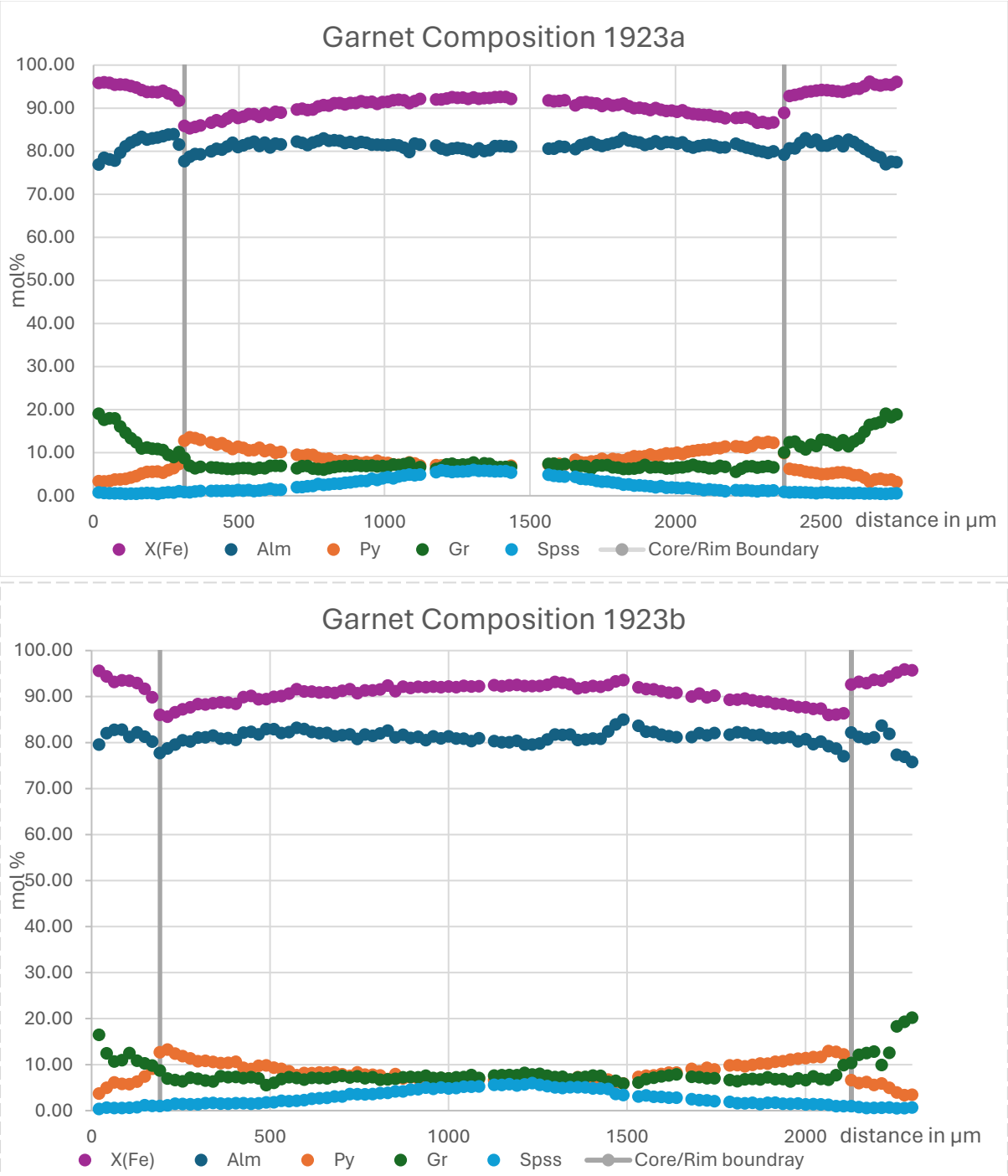

Figure 20: Garnet profiles of sample GM1923a and GM1923b. Both garnet profiles show almost the same trend in comparison. Gaps in the profile are caused by removed values.

Garnet sample 1923a is almandine rich with an average core composition of 81 mol.%. There is a clear core-rim chemical boundary, which, however, cannot be seen at the microscope. At the core-rim transition, the almandine content is 78 mol.%. The garnet rim displays an increase in almandine up to 84 mol.% followed by a gentle decrease to 78 mol.%. Pyrope content is low in the garnet core and steadily increases to 14 mol.% at the core-rim boundary, finally decreasing to 3 mol.% in rim. Spessartine continuously decrease from core to rim (7 mol.% to 1 mol.%). The grossular content is almost constant in garnet core (7 mol.%) and strongly increases in garnet rim up to 20 mol.%. The chemical profile measured in the garnet from sample 1923b is very similar to the one described one from sample 1923a. The only notable difference is alm exhibiting a small outer-core local maximum of 85%.

Several chemical analyses (n=17) were not considered along the analysed profiles and correspond to mixed analyses between the host garnet and inclusions.

6.2 Chloritoid

Chemical samples (n= 26) of chloritoid included in garnet and present in the matrix were analysed. Chloritoid included in different domains (i.e., core, mantle, rim) of garnet$_1$ shows a clear trend of increasing X_{Mg} (X_{Mg} = 0.16 – 0.21) from core to rim (red series in Figure 21 below). A similar, but more subtle, trend can be observed in chloritoid crystals included in garnet$_2$ (blue series in Figure 21 below) with an increase X_{Mg} = 0.17 – 0.18 from core to mantle. At the rim, however, X_{Mg} sharply decreases. X_{Mg} in the matrix are more evenly distributed and spread over all previous X_{Mg} ranges without a clear trend.

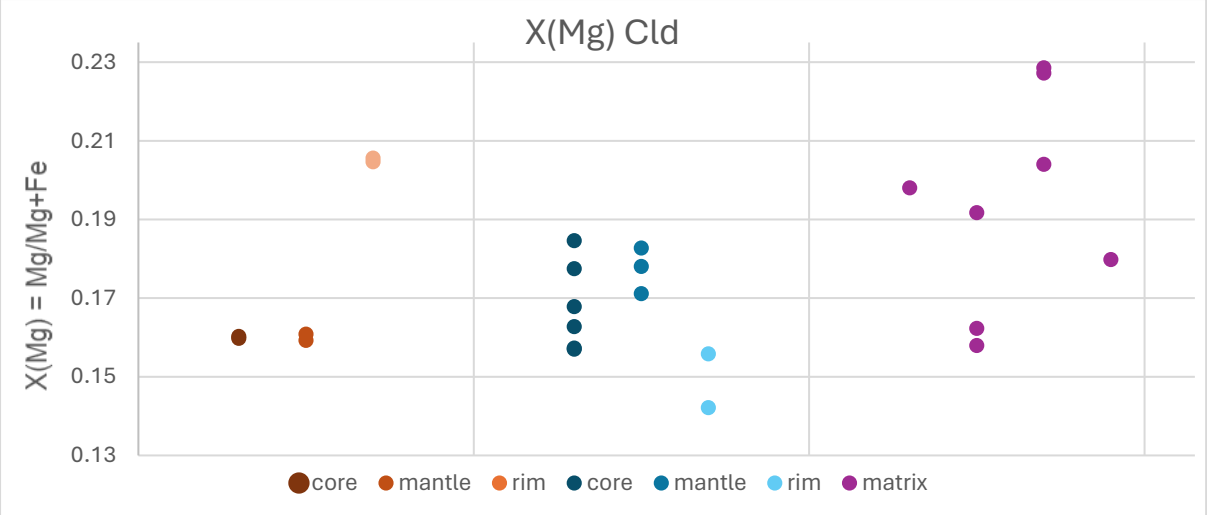

Figure 21: trends in X_{Mg} based on the position of the crystal. Red-shades and blue-shades show inclusions in different garnets. Different positions in the purple-shaded points correspond to different crystals in the matrix. Red points show a clear trend in X_{Mg} increase towards the rim while blue points show a reverse trend.

A table with examples of oxide percent and a.p.f.u. can be found in the appendix (table 4).

6.3 Chlorite

X_{Mg} trends in chlorite (n= 11) are less significant. Two neighbouring chlorites crystals which replaced glaucophane at the core display the same average X_{Mg} = 0.44 (red and blue in Figure 22). Chlorite present in the matrix displays a subtly lower X_{Mg} = 0.39. As they would have formed during the replacement stage, temperatures could have been more stable.

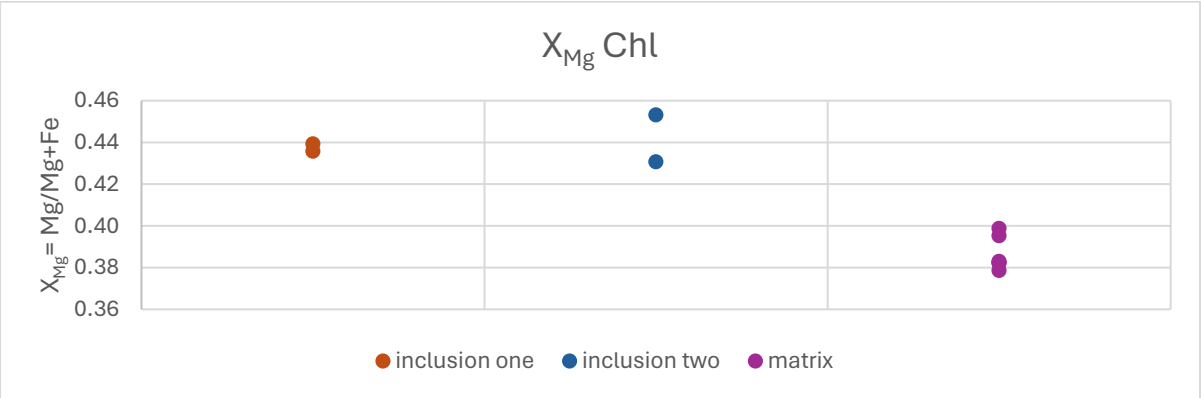

Figure 22: Red and blue shades correspond to different crystals. There is no significant trend.

A table with examples of oxide percent and a.p.f.u. can be found in the appendix (table 5).

6.4 Mica

Mica (n= 27) was analysed in different structural position. Due to a problem in the calibration of the microprobe, all measurements display lower K_2O content than expected resulting in a very low closure (i.e., 92% instead of 96%). The chemical analyses of mica are plotted and described below. However, the reliability of these data should be treated with caution.

Only one mica inclusion in garnet was measured and on this crystal six analyses have been done. Mica included in garnet displays an X_{Mg} = 0.56. Here, a clear trend between average inclusion and matrix values is observed (X_{Mg} = 0.54 – 0.66). Mica in the samples is relatively Si-rich (3.3 – 3.4 a.p.f.u.).

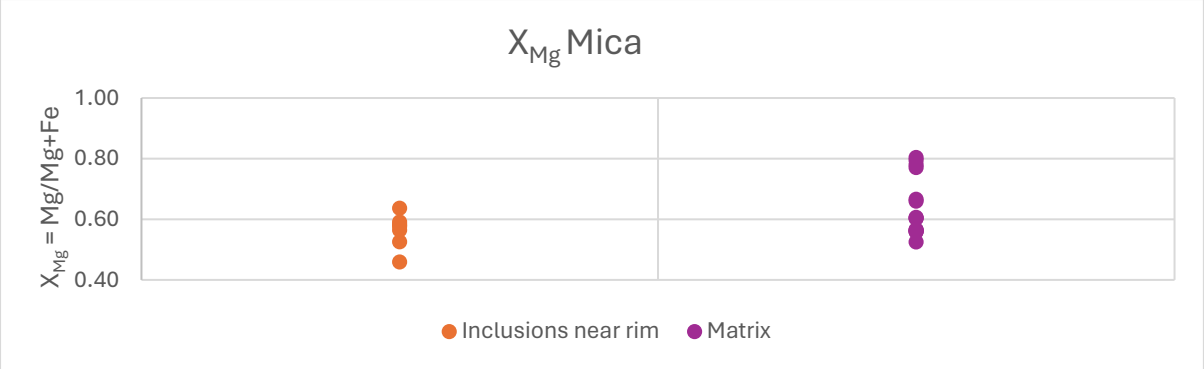

Figure 23: Mica X_{Mg} shows a clear trend.

A table with examples of oxide percent and a.p.f.u. can be found in the appendix (table 6).

7. Glaucophane Pseudomorphs

Two pseudomorphed glaucophane crystals were imaged by backscattered electron microscopy. Twenty-four quantitative microprobe analyses have been performed on the pseudomorphs to identify the minerals replacing glaucophane. This investigation reveals that glaucophane is replaced by an aggregate consisting of albite (n=5), chlorite (n=1) biotite (n=3) and amphiboles of the gedrite-anthopyllite-cummingtonite (GAC) family (n=5). Eleven analyses did not return good results and correspond to a mixing between different minerals. The pseudomorphs are, in fact, locally characterised by very fine-grained aggregates that cannot be precisely measured by microprobe analysis due to their extremely small size which is often well below 10 µm. In the following, a detailed description of the pseudomorphs is provided.

A table with examples of oxide percent and a.p.f.u. can be found in the appendix (Fig 7).

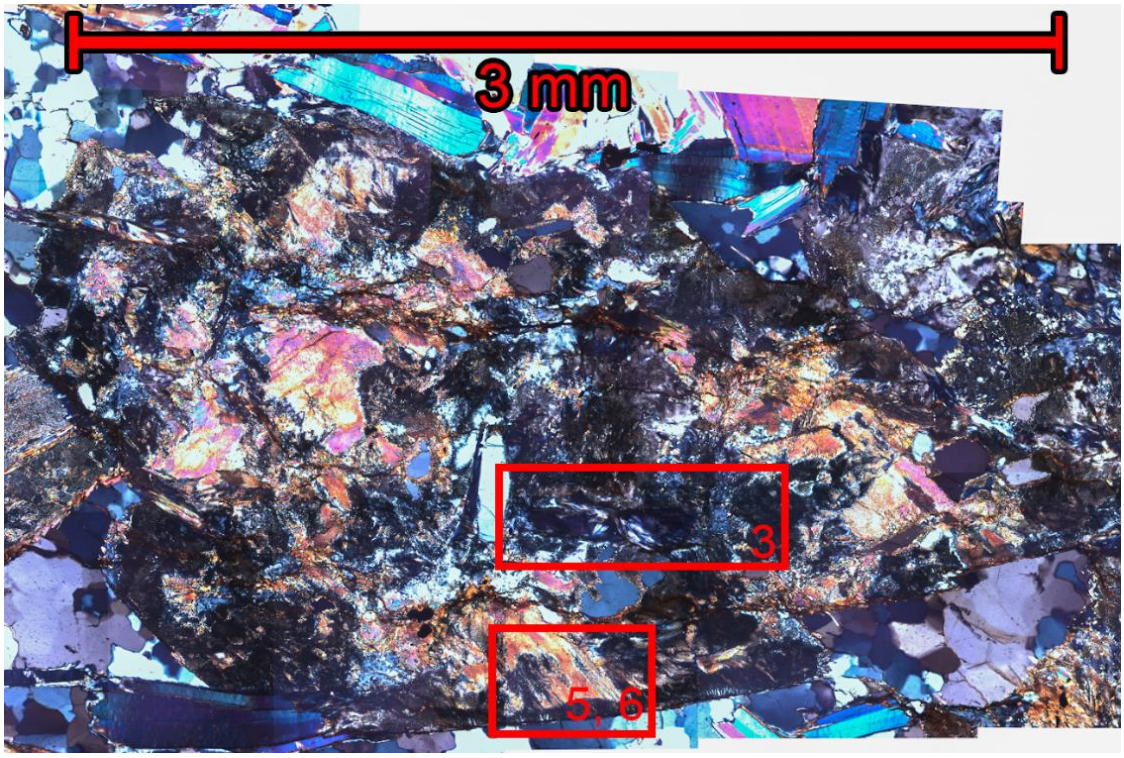

Figure 24: A multi-image stitch of glaucophane with relevant BSE images marked and numbered. In the appendix, a link to a full-resolution image corresponding to 80-megapixels can be found. BSE image three was taken but the corresponding chemical analysis was either lost or not performed.

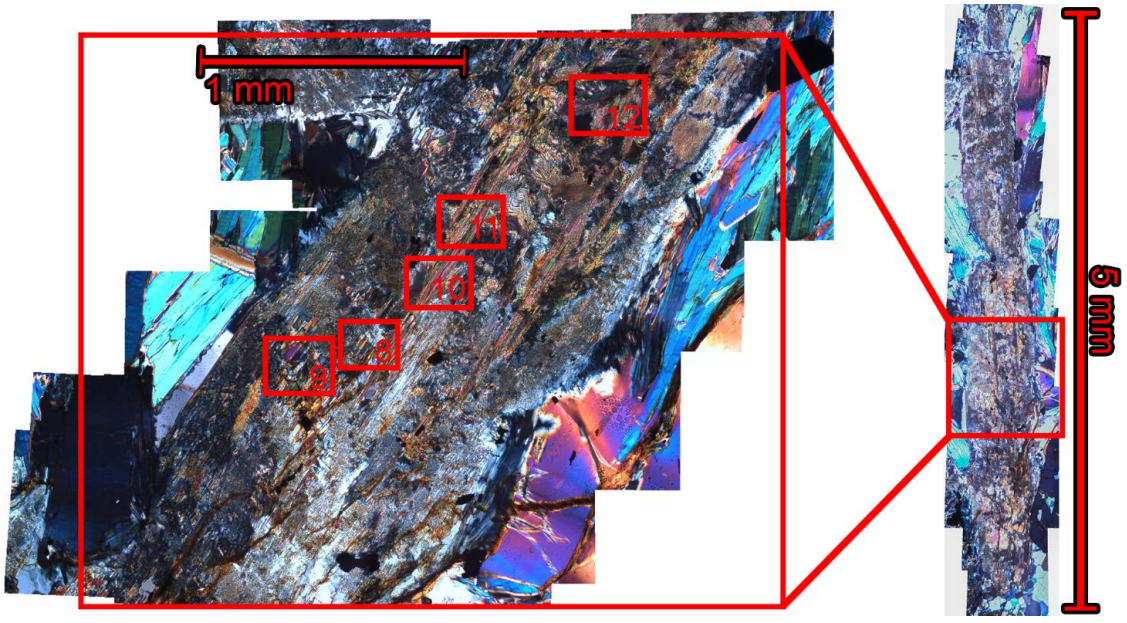

Figure 25: On the right, the entire, 5mm long, glaucophane crystal can be seen. The image on the left shows a zoom-in of the area where BSE images were taken. On the full-scale image provided in the appendix, individual biotite crystals can be seen.

7.1 Rim of Pseudomorphed Glaucophane One

BSE #5 and #6, points 1-9

BSE image #5 shows the external domain of a pseudomorphed glaucophane. In this domain, two different areas were investigated by microprobe analysis.

The first area (BSE image #6) corresponds to the outer rim of glaucophane and consists of very fine-grained aggregates of albite (points 1, 2, and 6, dark colour) and GAC (points 7,8, and 9, light grey). Points 3, 4, and 5 are mixed analyses. Crystals in this part of the rim are between 2-10 µm in diameter.

The second area corresponds to the inner rim of glaucophane. Here, most crystals are <5 µm. Albite (dark grey) occurs as elongated crystals up to 100 µm long. Because of the extremely small crystals and their intergrown texture, several points returned mixed results. Furthermore, points appear to have shifted. For example, 1 and 2 shifted slightly left while 6-9 appear to have shifted right.

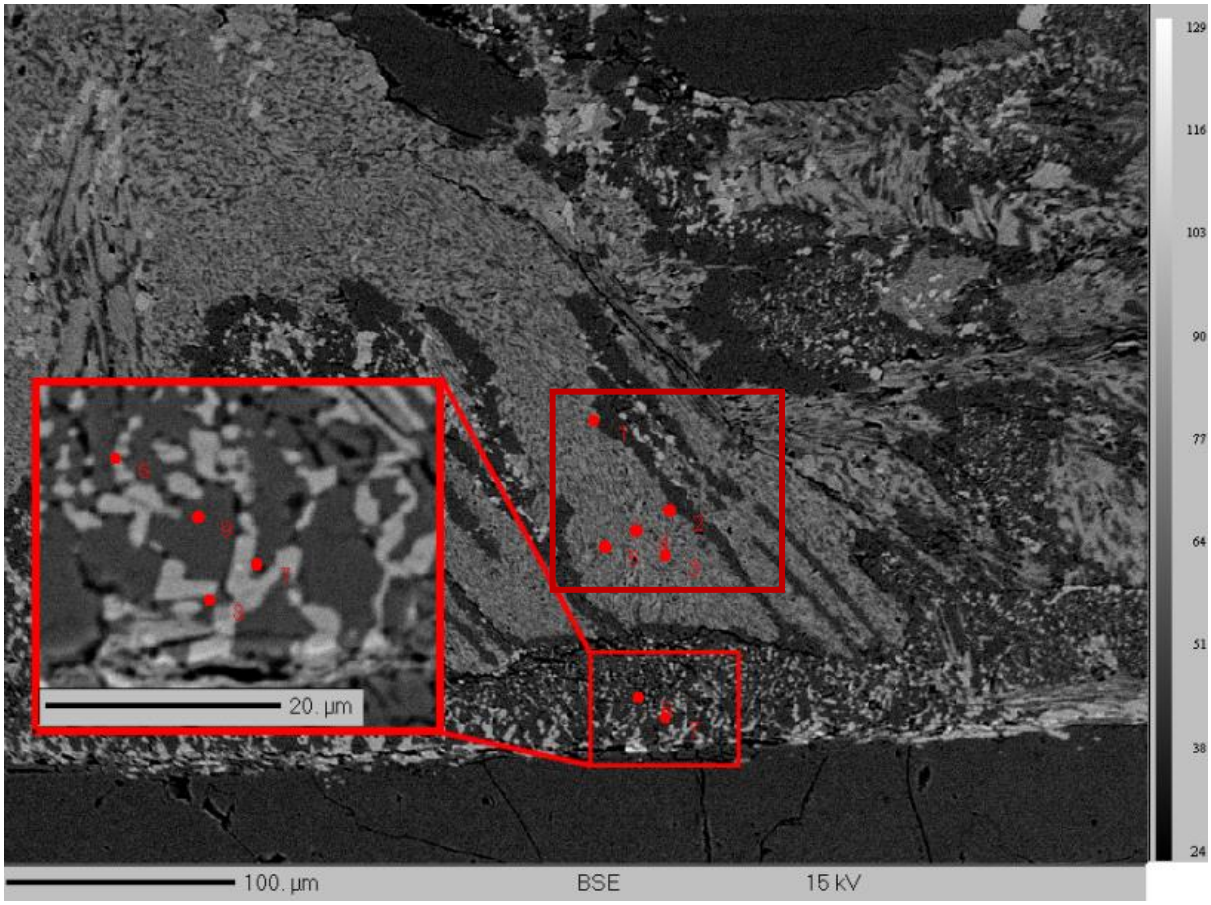

Figure 26: BSE image 6 clearly shows the point shift from the intended targets, however, the rim can still be identified as biotite and chlorite-free. Curiously, albite is darker than one might expect.

7.2 Core of Pseudomorphed Glaucophane Two

BSE #8, points 34-36

BSE image #8 shows the core of a different pseudomorphed glaucophane. Crystals in the core are generally more homogenous in size. The main minerals are biotite (point 34), GAC (point 35), and albite (point 36). Biotite and GAC show a preferred orientation parallel to the orientation of the pseudomorphed glaucophane and thus roughly perpendicular to the main strain direction.

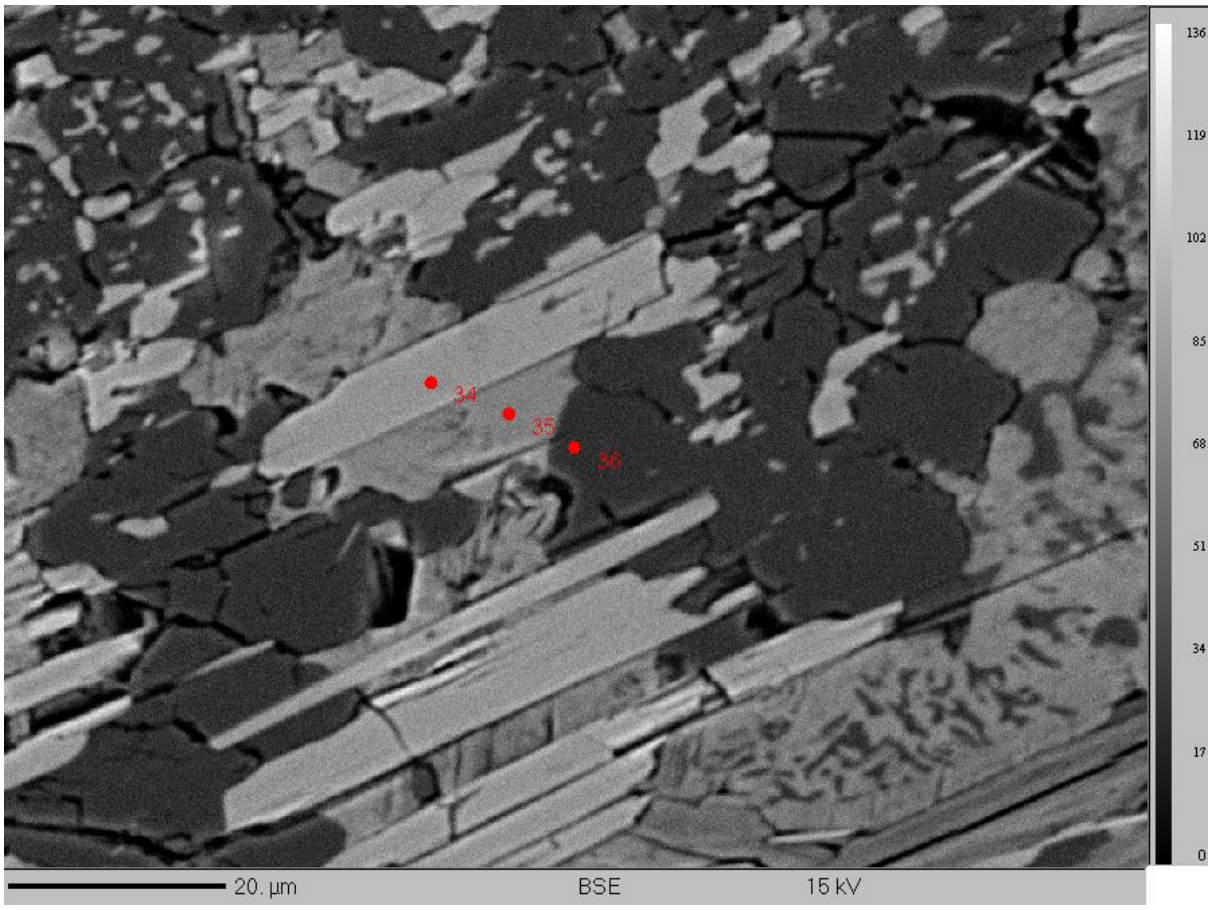

Figure 27: BSE image with three identifiable and unshifted points. For the following analysis, this was crucial as it allowed for BSE-colour-identification of minerals with shifted points.

BSE #9, points 37-39

BSE image #9 shows another area in the core of the pseudomorphed glaucophane two. This area is very similar to one of the BSE images #8 and consists of an aggregate of albite (point 37, dark grey) and GAC (point 38). Point 39 is a mixed analysis and illustrates the problem caused by the point-shift between biotite and GAC. It was measured at, what seems like, the border between a GAC and a biotite crystal judging by the BSE colour which is slightly darker than GAC. Biotite and GAC display similar shape preferred orientations.

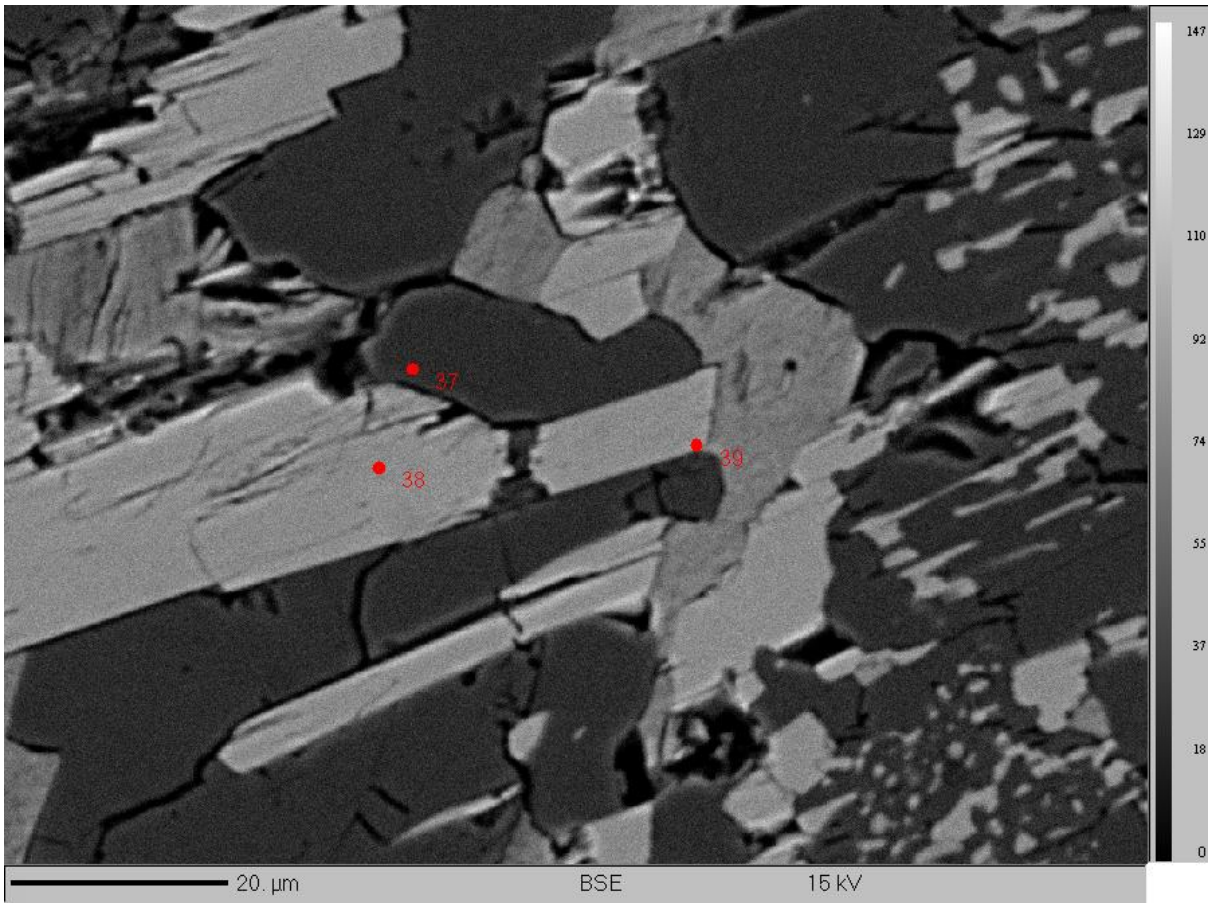

Figure 28: Another example of shifted points. However, identification by colour could be used to estimate modal amounts.

BSE #10, points 41-43 and BSE #11, points 44-46

BSE image #10 is a detail of the core of a pseudomorphed glaucophane. Here, all values returned mixed results. This is partly due to the shift of the points and the extremely small and intergrown crystals. Based on the chemical results one could argue that the analysed minerals are chloritised biotite as their Si-content is too high to be chlorite (43 wt.%), they contain significant K_2O (2.8 wt.%), but show a closure of around 90% like the one of chlorite.

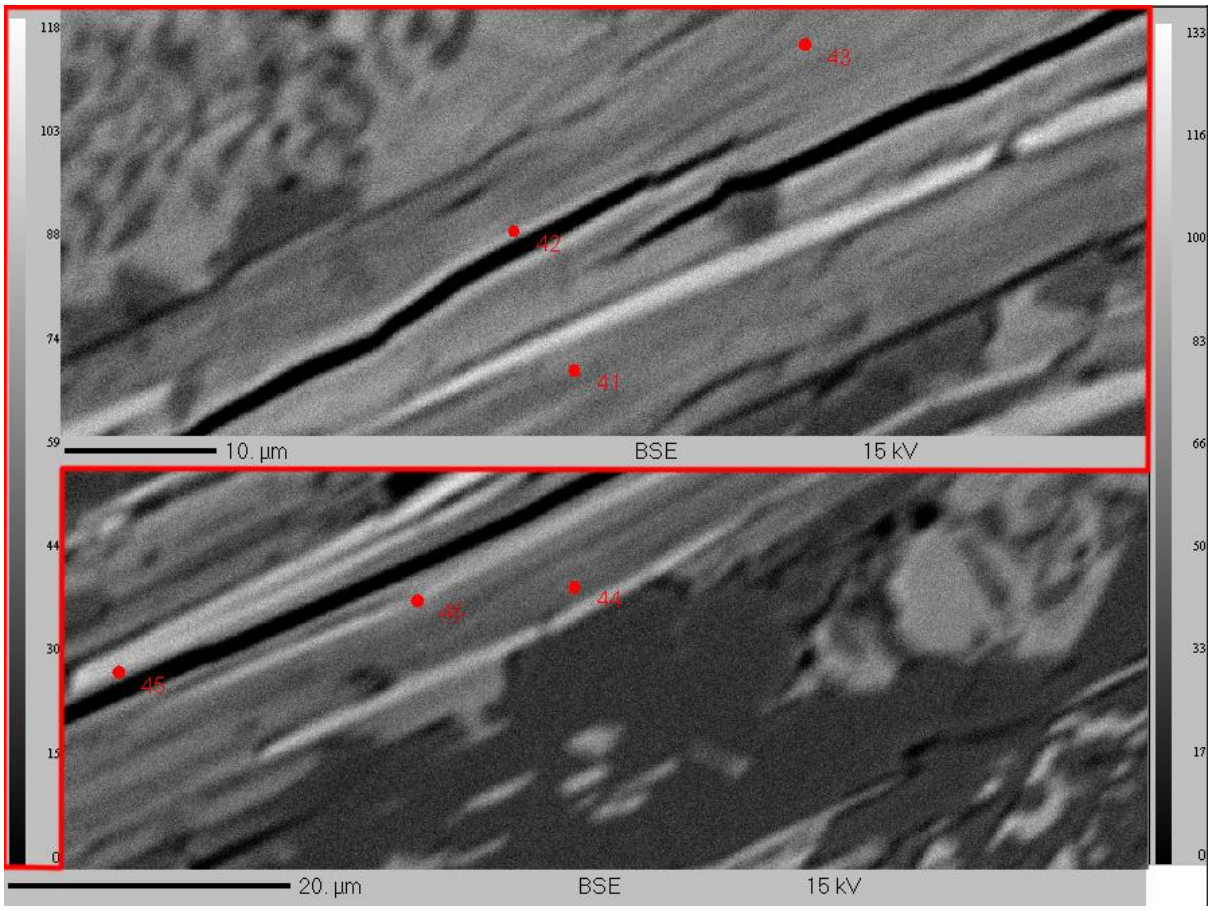

Figure 29: This image clearly shows the complex and intergrown structure. One cannot clearly make out any diagnostic colour, crystal borders are also not clearly defined.

BSE #12, points 47-49

BSE image #12 displays a domain in the core of a pseudomorphed glaucophane characterised by larger crystal size. This domain is surrounded by finer-grained aggregates. The points were chemically identified as biotite (points 47 and 48, light grey) and chlorite (point 49, dark grey).

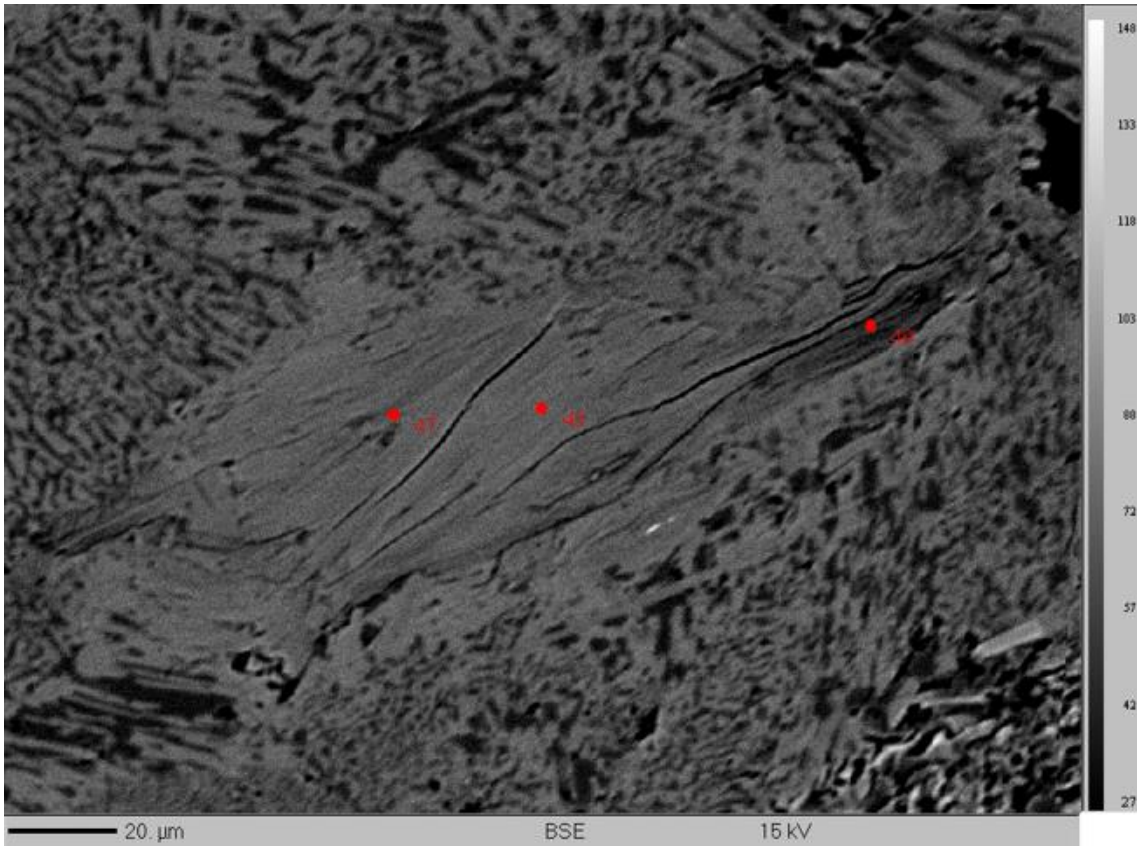

Figure 30: The points on the image were chemically identified as biotite. Curiously, they are slightly darker in colour than in the previous BSE images.

BSE #3, points 31-34

BSE image #12 has been taken in the core of a pseudomorphed glaucophane and displays an aggregate of coarse-grained phyllosilicates (light grey colour) surrounded by fine-grained crystals. In the coarse-grained domain, chlorite can be optically identified (see Figure 31). The presence of this relatively large domain dominated by chlorite proves that this mineral is a significant product of the chemical replacement of glaucophane.

Unfortunately, although some chemical analyses have been programmed in this domain, they were either lost or not performed correctly. Therefore, no chemical analyses of chlorite are available from this domain.

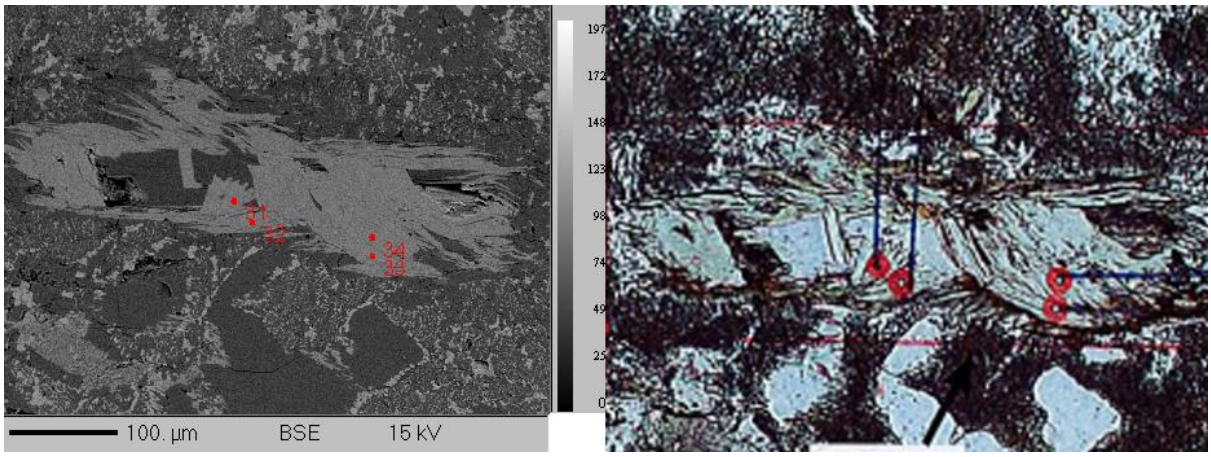

Figure 31: BSE image of chlorite which can be identified optically due to its colour. The similarity with those points which were interpreted as chloritised biotites becomes apparent.

8. Temperature calculation

A total of n=6 chloritoid inclusions were measured in a garnet where profile data was available.

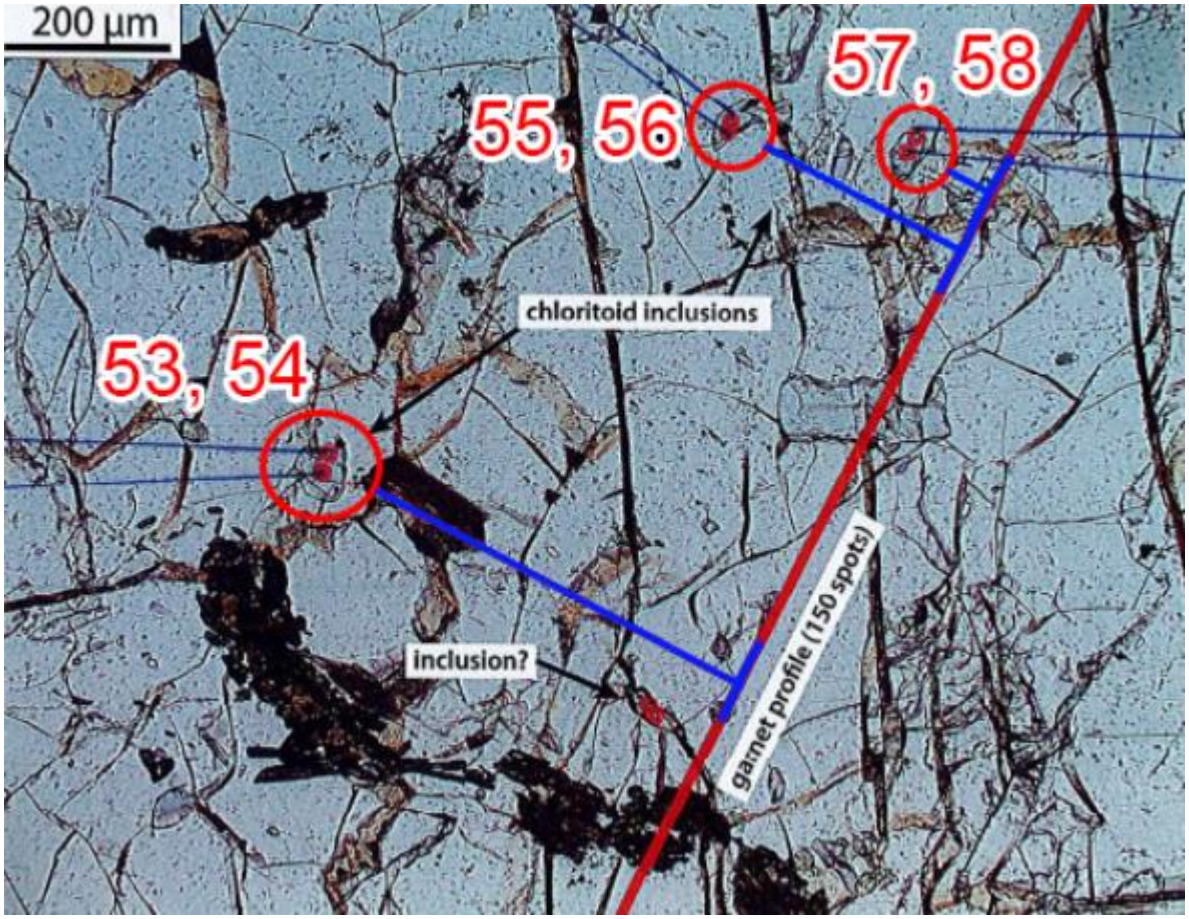

Figure 32: Microphoto with chloritoid measurements and garnet profile overlayed. The blue line marks the closest garnet value plus six in each direction. This was determined by pixel-counting.

Each measurement in the three crystals was paired with the two closest garnet measurements, plus six points to either side. This was done because calculated T-values varied greatly depending on which garnet measurement was chosen, and an average value was desirable. The decision to take six values to either side was made because some measurements along the profile returned non-garnet values and therefore had to be removed. It turned out that six values "away" from the two closest garnet points was possible for all chloritoid points.

From the n=84 calculated temperatures; the total average is 562 °C with a standard deviation of 22 °C. The average temperatures when looking at each chloritoid point individually were relatively similar with 57=559 °C, 58=561 °C, 55= 558 °C, 56= 562 °C, 54= 565 °C and 55= 567 °C. It should be noted, however, that the standard deviation for 54 and 55 is 33 °C while being only 16 °C for the rest of the calculations.

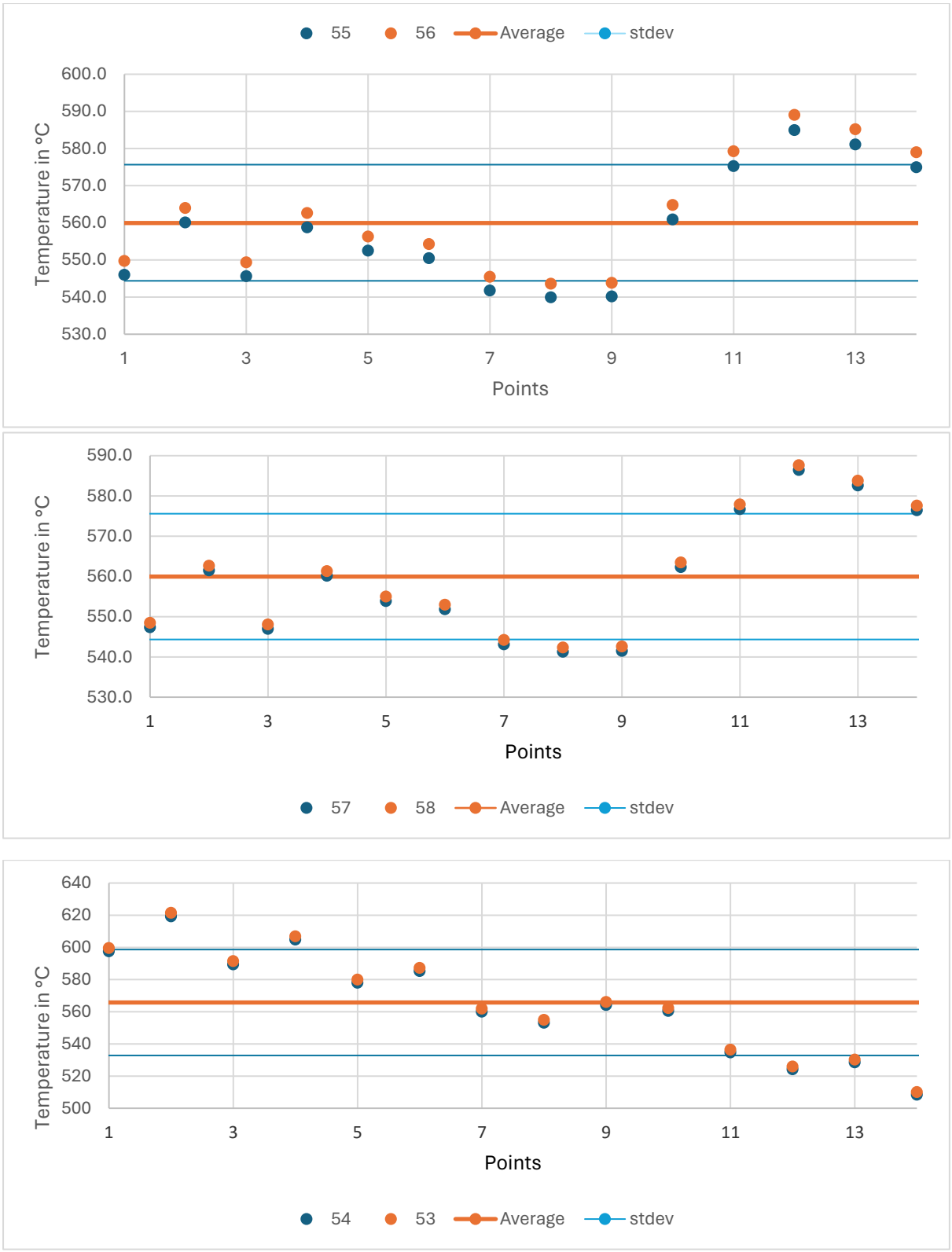

Figure 33: Results of temperature calculation. X=7 and X=8 correspond to the closest points to each chloritoid crystal. The necessity of using an average becomes clear when analysing the data-spread.

9. Discussion

9.1 Pseudomorphs after glaucophane in metapelites: chemical reactions

A peculiar characteristic of the investigated garnet micaschist is the presence of large pseudomorphed glaucophane crystals, overgrowing the main foliation. The main minerals replacing glaucophane are albite, GAC, chlorite and biotite. These minerals are stable at low-grade metamorphic conditions (greenschist-facies) suggesting that the consumption of glaucophane occurred during the exhumation path of the Muret Unit (i.e. < 10 kbar and < 500 °C) (Nosenzo et. al. 2022).

BSE images show that the texture of glaucophane pseudomorphs are quite complex with domains displaying different grain sizes, mineralogical content and modal amount. These observations suggest that different chemical reactions involving glaucophane consumption may have occurred.

There are several possible chemical reactions that could have consumed glaucophane during the corresponding metamorphism. Some possible reactions include:

$glaucophane = 2\ albite + chlorite$	(Miyashiro and Banno, 1958)	1
$5\ glaucophane + 3\ paragonite + 4\ water = 13\ albite + 3\ chlorite + quartz$	(Emond and Beunk, 1976) (Basora, Jenkins and Bish, 2012)	2
$25\ glaucophane + 6\ epidote + 7\ quartz + 14\ H_2O = 50\ albite + 9\ chlorite$	(Miyashiro and Banno, 1958)	3
$glaucophane + epidote = chlorite + albite$	(Schliestedt and Matthews, 1987), unbalanced	4
$glaucophane + chloritoid = paragonite + garnet + chlorite$	(Guiraud, Holland and Powell, 1990), unbalanced	5
$glaucophane + paragonite + garnet = albite + chlorite$	(Guiraud, Holland and Powell, 1990), unbalanced	6
$glaucophane + phengite + (quartz) = albite + chlorite + biotite$	(Koons and Thompson, 1985), unbalanced	7
$pumpellyite + glaucophane + quartz + water = actinolite + chlorite + albite$	(Tang and Zhang, 2013), unbalanced	8

Table 2: Possible glaucophane breakdown reactions.

All these reactions contain phases that have been identified in the investigated sample. However, reaction 8 also involves pumpellyite, a mineral not observed in the studied sample. Pumpellyite is quite rare in metapelites and is a typical mineral of metabasite equilibrated at greenschist-facies conditions (Tang and Zhang, 2013).

Epidote is a minor component of metapelites, and it is present in minor abundance in the investigated rock. Therefore, reactions 3 and 4 are also unlikely.

Reactions 1, 2, 5, 6 and 7 are all possible reactions that may have occurred consuming glaucophane. However, these reactions do not produce Fe-Mg amphibole, a mineral commonly observed in the pseudomorph (previously labelled GAC).

One approach to gain a deeper understanding of which of these reactions is a possible reaction that occurred in the analysed rocks, is to estimate modal amounts of product minerals to aid with stoichiometric balancing. This was done graphically by analysing the minerals that were identified chemically and matching them with their respective colour in the BSE image. Then, the same method used in section 3.1 was applied. This analysis can only be carried out in those images that have clear crystal borders, images with significant intergrowth cannot be counted reliably.

BSE	Rim/core	Albite	Biotite	GAC
#6	Rim	77	0	17
#8	Core	56	23	20
#9	Core	60	9	30

Table 3: Estimated modal amounts based on BSE images. These numbers, if more BSE images were available, could be used to aid stoichiometric balancing. However, there might be a sampling bias introduced since BSE image locations are chosen based on mineral of interest, not even spread.

The modal amounts show that there is no biotite in the rim and that albite and GAC are by far the most abundant. Biotite appears to only exist in small amounts. Furthermore, albite decreases towards the core while GAC increases. As mentioned above, there is no chemical analyses for chlorite that could be included in this table. However, it can be optically determined that chlorite constitutes a significant proportion of the product.

Based on the minerals analysed, the unbalanced reaction

$$glaucophane = albite + (Fe, Mg)\ amphibole + chlorite + biotite + quartz$$

would be expected. However, this does not appear to be a valid chemical reaction as it cannot be balanced stoichiometrically. This leads to the conclusion that there must be unaccounted-for reactants or products. Immediately, the excess of Mg/Fe on the product side becomes obvious. This could be solved by adding Talc as a reactant.

$$glaucophane + talc = albite + (Fe, Mg)\ amphibole + chlorite + biotite + quartz$$

However, even with the addition of talc the reaction remains unbalanced, though the discrepancy between products and reactant is significantly lower.

Figures 36, 37 and 38, better visible in the appendix, nicely visualise the complexity of the glaucophanes. Different domains within one single crystal clearly show different dominant product minerals. It can, therefore, be assumed, that no single chemical reaction took place in the whole crystal. In other words, different chemical reactions plausibly took place at the micrometre scale producing different minerals.

9.2 Pseudomorphs after glaucophane in metapelites: no evidence for late heating

The minerals observed in the pseudomorphs (chlorite, albite, biotite, Fe-Mg amphibole) are typical of greenschist facies metamorphic conditions. The presence of biotite in the pseudomorph suggests that its growth is controlled by the local bulk chemistry (Manzotti et al., 2018). Chlorite requires significant amounts of water to form. Through continuous chlorite growth, water availability decreases. As biotite requires less water to grow, this depletion starts to favour biotite growth making it a significant product during retrogression. Thus, biotite may have grown at greenschist-facies metamorphic conditions rather than higher P-T conditions indicative of slab break-off. Typical greenschist conditions, where this could have taken place instead, are 300–400 °C and 2-6 kbar (Winter, 2014).

According to these observations, the mineral products of glaucophane breakdown do not support the suggested heating at 0.5 GPa suggested by Campomenosi et al. (2021) or Minghardi et al. (2023) during exhumation in the Muret-Unit. The absence of staurolite in the studied rock, a mineral commonly stable in metapelites at these P-T conditions, is in line with this conclusion.

The mineral products identified in glaucophane pseudomorphs are therefore compatible with an isothermal decompression (Fig. 34a) and do not support a late heating stage at low pressure. Consequently, there is no evidence of slab break-off in the investigated sample.

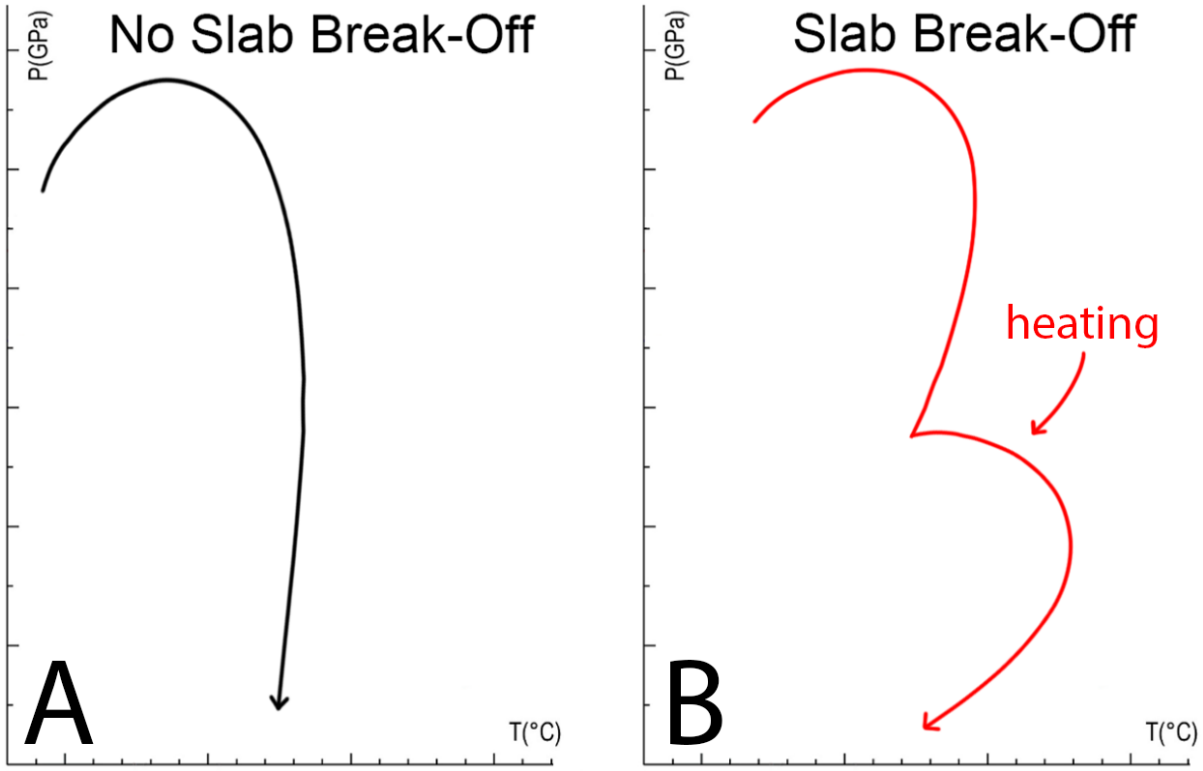

Figure 34: Exaggerated P-T paths for no slab break-off vs. slab break-off. The observed mineral assemblages do not support late heating at low P.

9.3 Strain history recorded in garnet

Garnets in the analysed samples are generally of similar size and do not appear to be optically zoned. Data from two garnet profiles contain no evidence of two-generation garnet growth. It can therefore be assumed that garnets in the studied samples are single-generation (Manzotti et al., 2024).

Inclusions in garnet are randomly oriented and can therefore not be used to analyse early-stage strain direction. There are no microstructures that resemble internal deformation, and no other signs of garnet rotation is visible.

The cracks in garnet, which are offset at 45° towards the main foliation and could be interpreted as recording the strain direction, could have formed during two processes – strain during burial or release of strain during exhumation. There are some key observations to consider. Firstly, most cracks are joints, meaning that there is no displacement. These cracks are only oxidised at their rims and do not show any filling or other reactions. Other garnet cracks which opened laterally, are filled with chlorite. If these cracks had formed during an earlier stage, one would expect prograde, high-pressure minerals such as garnet, to fill them. Examples of this can be found in Giuntoli, Lanari and Engi (2017) or Manzotti et. al. (2024).

Here, early-stage garnet cracks were filled by Alpine garnet of different compositions sealing the cracks. If present, this would be evidence suggesting early-stage fracturing in the sample.

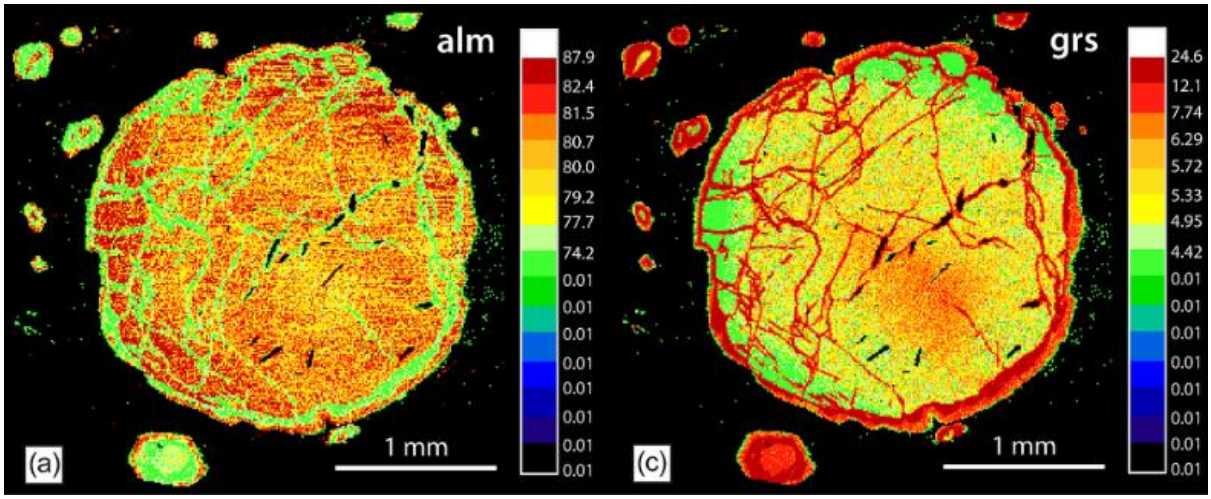

Figure 35: Example of garnet-filled garnet cracks (Manzotti et. al. 2024).

Though no such chemical analysis was performed directly, the visual evidence suggests oxidisation only. The garnet profiles also show no sign of garnet-filled cracks.

By contrast, the coexistence of chlorite-filled cracks and joints with oxidised edges suggests that the fracturing occurred during later stages. Cracks likely formed during exhumation as a cause of stress release. Cracks filled with chlorite must have formed when the rock was in the greenschist facies. It could be argued that oxidised cracks formed much later as they remained unfilled.

9.4 Garnet chemistry and Alpine metamorphism in the Muret Unit

Sample GM13 in Nosenzo et. al. (2022 and 2023) was collected close to samples GM1923 investigated in this paper. These two samples display nearly identical peak mineral assemblages, consisting of q-grt-ctd-gln-chl-ms-law-rt. All minerals, apart from lawsonite, were observed in GM1923.

However, a key difference between these two samples is the large amount of glaucophane overgrowing the main foliation in sample GM1923 and the absence of polycyclic garnet in this sample which can, by contrast, be found in GM13.

Since garnets in GM13 consist of pre-Alpine cores and Alpine rims, it only makes sense to compare the rim of GM13 with the garnet profiles from this paper. And indeed, they are strikingly similar. Both show alm (~80 mol%) and spss (<5 mol%). Py and gr, which both plot at around 10% for GM13, are at ~4% and 18% in GM1923 respectively. Logically, values beyond the pre-Alpine to Alpine transition are significantly different between the samples. It is reported that Alpine garnet started growing at 18–19 kbar ~480 °C and

peaked at 19–22 kbar 530 °C–550 °C. The studies cited report good matching between the observed and the modelled values Nosenzo et. al. (2023). The peak temperature somewhat correlates with the temperature calculated here.

The difference in the Alpine garnet chemistry between the investigated sample (GM1923) and the sample (GM13) studied by Nosenzo et al. (2022 and 2023) may suggest that garnet grew at different P-T conditions along the same P-T path. Further investigations are needed to reconstruct the P-T path followed by sample GM1923 and the P-T conditions at which the Alpine garnet grew.

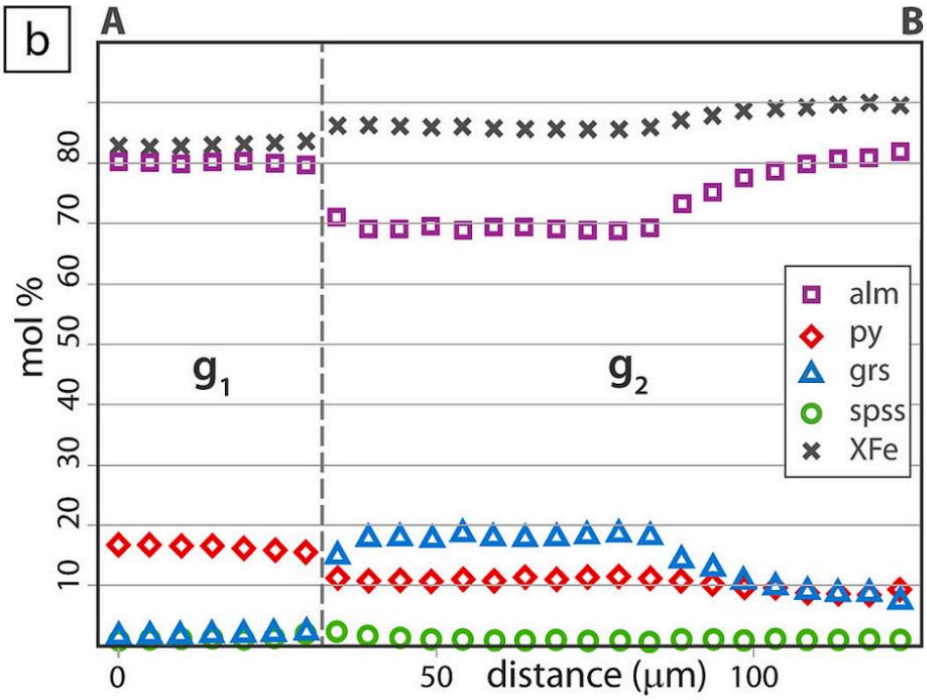

Figure 36: Garnet profile from GM13 where g_1 is pre-Alpine and g_2Alpine garnet. Similarities are clearly visible (Nosenzo et. al., 2023)

In the studied sample (GM1923), a temperature of 560°C for garnet growth was calculated using the garnet-chloritoid thermometer. Chloritoid measurements were arguably limited (n=6) and thus, it can be argued that results lack statistical significance. It would have been favourable to compare the garnet-chloritoid thermometry results with other thermometers like garnet-ilmenite (Feenstra and Engi, 1998), for example. However, necessary ilmenite analyses were not taken in the relevant garnet.

Nevertheless, the calculated temperature for sample GM1923 is in good agreement with previous estimates on garnet-chloritoid micaschist in the Muret Unit (Nosenzo et al., 2023).

10. Conclusions

This study leads to the following conclusions:

- In the studied micaschist, Alpine garnet grew at 562 ± 22 °C, in agreement with previous studies in the Muret Unit.
- The minerals replacing glaucophane (chlorite, albite, biotite, Fe-Mg amphibole) are indicative of greenschist facies metamorphic conditions (< 500 °C) and developed during the exhumation of the Muret Unit.
- This mineral assemblage does not support a stage of late heating at low pressure as recently suggested by some authors.

11. Implications and prospects

Despite the rather limited data availability for temperature calculations and the loss of data, the temperature calculated in this paper matches well with the temperature modelled by Nosenzo et. al. (2022 and 2023). It would be desirable to recover lost data and redo analyses for minerals that would allow for cross reference like garnet-ilmenite.

The same goes for glaucophane pseudomorphs. Here, it would be desirable to redo those measurements that returned mixed values. Furthermore, more detailed chemical analysis that give a deeper understanding of total glaucophane composition could help to narrow down the chemical reactions involved and potentially allow for PT estimation of the retrograde metamorphism.

More analyses and calculations need to be made to gain a more solid understanding of P-T conditions.

11. Acknowledgements

I would like to express my deepest gratitude to my supervisor Paola Manzotti. Her support, patience and expertise were invaluable throughout the entire process and our discussions significantly deepened my understanding of, and interest in this area of research. I would like to especially thank her for her help deciphering the data sets and corresponding measurements, and her feedback to my texts and calculations.

13. Reference list

André Michard, Schmid, S.M., Abdeltif Lahfid, Ballèvre, M., Manzotti, P., Chopin, C., Iaccarino, S. and Dana, D. (2022). The Maira-Sampeyre and Val Grana Allochthons (south Western Alps): review and new data on the tectonometamorphic evolution of the Briançonnais distal margin. *Swiss Journal of Geosciences*, 115(1). doi:https://doi.org/10.1186/s00015-022-00419-8.

Avigad, D., Chopin, C. and Le Bayon, R. (2003). Thrusting and Extension in the Southern Dora-Maira Ultra-High-Pressure Massif (Western Alps): View from Below the Coesite-Bearing Unit. *The Journal of Geology*, 111(1), pp.57–70. doi:https://doi.org/10.1086/344664.

Balestro, G., Nosenzo, F., Cadoppi, P., Fioraso, G., Groppo, C. and Festa, A. (2020). Geology of the southern Dora-Maira Massif: insights from a sector with mixed ophiolitic and continental rocks (Valmala tectonic unit, Western Alps). *Journal of Maps*, 16(2), pp.736–744. doi:https://doi.org/10.1080/17445647.2020.1824825.

Basora, A.M., Jenkins, D.M. and Bish, D.L. (2012). The lower-pressure stability of glaucophane in the presence of paragonite and quartz in the system Na2O-MgO-Al2O3-SiO2-H2O. *The American mineralogist*, [online] 97(4), pp.713–726. doi:https://doi.org/10.2138/am.2012.3931.

Bonnet, G., Chopin, C., Locatelli, M., Kylander-Clark, A. and Hacker, B.R. (2022). Protracted Subduction of the European Hyperextended Margin Revealed by Rutile U-Pb Geochronology Across the Dora-Maira Massif (Western Alps). *Tectonics*, 41(4). doi:https://doi.org/10.1029/2021tc007170.

Bucher, K. (2005). METAMORPHIC ROCKS | Facies and Zones. *Encyclopedia of Geology*, pp.402–409. doi:https://doi.org/10.1016/b0-12-369396-9/00319-1.

Campomenosi, N., Scambelluri, M., Angel, R.J., Hermann, J., Mazzucchelli, M.L., Boriana Mihailova, Piccoli, F. and Alvaro, M. (2021). Using the elastic properties of zircon-garnet host-inclusion pairs for thermobarometry of the ultrahigh-pressure Dora-Maira whiteschists: problems and perspectives. *Contributions to mineralogy and petrology*, 176(5). doi:https://doi.org/10.1007/s00410-021-01793-6.

Chopin, C. (1984). Coesite and pure pyrope in high-grade blueschists of the Western Alps: a first record and some consequences. *Contributions to Mineralogy and Petrology*, 86(2), pp.107–118. doi:https://doi.org/10.1007/bf00381838.

Chopin, C., Henry, C. and Michard, A. (1991). Geology and petrology of the coesite-bearing terrain, Dora Maira massif, Western Alps. *European Journal of Mineralogy*, 3(2), pp.263–292. doi:https://doi.org/10.1127/ejm/3/2/0263.

Coleman, R.G. (1967). Glaucophane schists from california and new caledonia. *Tectonophysics*, 4(4-6), pp.479–498. doi:https://doi.org/10.1016/0040-1951(67)90012-1.

Compagnoni, R. and Rolfo, F. (2003). UHPM Units in the Western Alps. *EMU Notes Mineral*, pp.13–49.

David J.A. Jenkins and Juan Carlos Corona (2006). The role of water in the synthesis of glaucophane. *American Mineralogist*, 91(7), pp.1055–1068. doi:https://doi.org/10.2138/am.2006.2014.

Deer, W.A., Howie, R.A. and J Zussman (2013). *An introduction to the rock-forming minerals*. London: The Mineralogical Society.

Emond and Beunk, F.F. (1976). Blue amphibole-albite-chlorite assemblages from Fuscaldo (S Italy) and the role of glaucophane in metamorphism. *Contributions to mineralogy and petrology*, 58(3), pp.221–234. doi:https://doi.org/10.1007/bf00402353.

Feenstra, A. and Engi, M. (1998). An experimental study of the Fe-Mn exchange between garnet and ilmenite. *Contributions to Mineralogy and Petrology*, 131(4), pp.379–392. doi:https://doi.org/10.1007/s004100050399.

Ford, M., Stéphanie Duchêne, Gasquet, D. and Olivier Vanderhaeghe (2006). Two-phase orogenic convergence in the external and internal SW Alps. *Journal of the Geological Society*, 163(5), pp.815–826. doi:https://doi.org/10.1144/0016-76492005-034.

Ghent, E.D., Stout, M.Z. and Black, P.M. (1987). Chloritoid-bearing rocks associated with blueschists and eclogites, northern New Caledonia. *Journal of metamorphic geology*, 5(2), pp.239–254. doi:https://doi.org/10.1111/j.1525-1314.1987.tb00382.x.

Mingardi Giulia, Campomenosi, N., Gilio, M., Chopin, C., Scambelluri, M. and Alvaro, M. (2023). Elastic thermobarometry of ultrahigh-pressure metapelites from the Brossasco-Isasca Unit (Dora-Maira Massif, Western Alps). Lithos, 448-449(448-449), pp.107167–107167. doi:https://doi.org/10.1016/j.lithos.2023.107167.

Giuntoli, F., Lanari, P. and Engi, M. (2017). Deeply subducted continental fragments: I. Fracturing, dissolution-precipitation and diffusion processes recorded by garnet textures of the central Sesia Zone (Western Italian Alps). *Solid Earth Discussions*. [online] doi:https://doi.org/10.5194/se-2017-87.

Grambling, J.A. (1983). Reversals in Fe-Mg partitioning between chloritoid and staurolite. *American Mineralogist*, 68(68), pp.373–388.

Groppo, C., Ferrando, S., Gilio, M., Botta, S., Nosenzo, F., Balestro, G., Festa, A. and Rolfo, F. (2019). What's in the sandwich? New P-T constraints for the (U)HP nappe stack of southern Dora-Maira Massif (Western Alps). *European Journal of Mineralogy*, 31(4), pp.665–683. doi:https://doi.org/10.1127/ejm/2019/0031-2860.

Guiraud, M., Holland, B. and Powell, R. (1990). Calculated mineral equilibria in the greenschist-blueschist-eclogite facies in Na2O?FeO?MgO?Al2O3?SiO2?H2O. *Contributions to Mineralogy and Petrology*, 104(1), pp.85–98. doi:https://doi.org/10.1007/bf00310648.

Ji, S., Zhao, P. and Saruwatari, K. (1997). Fracturing of garnet crystals in anisotropic metamorphic rocks during uplift. *Journal of Structural Geology*, [online] 19(5), pp.603–620. doi:https://doi.org/10.1016/S0191-8141(97)00006-0.

Koons, P.O. and Thompson, A.B. (1985). Non-mafic rocks in the greenschist, blueschist and eclogite facies. *Chemical Geology*, 50(1-3), pp.3–30. doi:https://doi.org/10.1016/0009-2541(85)90109-3.

Le Breton, E., Brune, S., Ustaszewski, K., Zahirovic, S., Seton, M. and R. Dietmar Müller (2021). Kinematics and extent of the Piemont–Liguria Basin – implications for subduction processes in the Alps. *European Geoscience Union*, 12(4), pp.885–913. doi:https://doi.org/10.5194/se-12-885-2021.

M. Moazzen (2004). CHLORITE-CHLORITOID-GARNET EQUILIBRIA AND GEOTHERMOMETRY IN THE SANANDAJ-SIRJAN METAMORPHIC BELT, SOUTHERN IRAN. *Iranian Journal of Science and Technology (Sciences)*, 28(1), pp.65–78. doi:https://doi.org/10.22099/ijsts.2004.2835.

Manzotti, P., Bosse, V., Pitra, P., Robyr, M., Schiavi, F. and Ballèvre, M. (2018). Exhumation rates in the Gran Paradiso Massif (Western Alps) constrained by in situ U–Th–Pb dating of accessory phases (monazite, allanite and xenotime). Contributions to Mineralogy and Petrology, 173(3). doi:https://doi.org/10.1007/s00410-018-1452-7.

Manzotti, P., Regis, D., Petts, D.C., Graziani, R. and Polivchuk, M. (2024). Formation of multistage garnet grains by fragmentation and overgrowth constrained by microchemical and microstructural mapping. *Journal of metamorphic geology*, 42(4), pp.471–496. doi:https://doi.org/10.1111/jmg.12761.

Manzotti, P., Schiavi, F., Nosenzo, F., Pitra, P. and Ballèvre, M. (2022). A journey towards the forbidden zone: a new, cold, UHP unit in the Dora-Maira Massif (Western Alps). *Contributions to mineralogy and petrology*, 177(6). doi:https://doi.org/10.1007/s00410-022-01923-8.

Miyashiro, A. and Banno, S. (1958). Nature of glaucophanitic metamorphism. *American Journal of Science*, [online] 256(2), pp.97–110. doi:https://doi.org/10.2475/ajs.256.2.97.

Nosenzo, F., Manzotti, P., Krona, M., Ballèvre, M. and Poujol, M. (2024). Tectonic architecture of the northern Dora-Maira Massif (Western Alps, Italy): field and geochronological data. *Swiss journal of geosciences*, 117(1). doi:https://doi.org/10.1186/s00015-024-00459-2.

Nosenzo, F., Manzotti, P., Poujol, M., Ballèvre, M. and Langlade, J. (2022). A window into an older orogenic cycle: *P–T* conditions and timing of the pre-Alpine history of the Dora-Maira Massif (Western Alps). *Journal of metamorphic geology*, 40(4), pp.789–821. doi:https://doi.org/10.1111/jmg.12646.

Nosenzo, F., Manzotti, P. and Robyr, M. (2023). H2O budget and metamorphic re-equilibration in polycyclic rocks as recorded by garnet textures and chemistry. *Lithos*, 452-453, pp.107230–107230. doi:https://doi.org/10.1016/j.lithos.2023.107230.

Perchuk, L.L. (1991). *Progress in Metamorphic and Magmatic Petrology*. Cambridge University Press.

Pownceby, M.I., Wall, V.J. and St, H. (1991). An experimental study of the effect of Ca upon garnet-ilmenite Fe-Mn exchange equilibria. *American Mineralogist*, 76(74), pp.1580–1588.

Schliestedt, M. and Matthews, A. (1987). Transformation of blueschist to greenschist facies rocks as a consequence of fluid infiltration, Sifnos (Cyclades), Greece. *Contributions to Mineralogy and Petrology*, 97(2), pp.237–250. doi:https://doi.org/10.1007/bf00371243.

Stallard, A. and Shelley, D. (2005). The initiation and development of metamorphic foliation in the Otago Schist, Part 1: competitive oriented growth of white mica. *Journal of Metamorphic Geology*, 23(6), pp.425–442. doi:https://doi.org/10.1111/j.1525-1314.2005.00587.x.

Tang, X.-C. and Zhang, K.-J. (2013). Lawsonite- and glaucophane-bearing blueschists from NW Qiangtang, northern Tibet, China: mineralogy, geochemistry, geochronology, and tectonic implications. *International Geology Review*, 56(2), pp.150–166. doi:https://doi.org/10.1080/00206814.2013.820866.

Tracy, R. and Robinson, P. (1976). Garnet composition and zoning in the determination of temperature and pressure of metamorphism, central Massachusetts. *American Mineralogist*, 61, pp.762–775.

Vidal, O., Goffe, G., Bousquet, R. and Parra, T. (1999). Calibration and testing of an empirical chloritoid-chlorite Mg-Fe exchange thermometer and thermodynamic data for daphnite. *Journal of Metamorphic Geology*, 17(1), pp.25–39. doi:https://doi.org/10.1046/j.1525-1314.1999.00174.x.

von Blanckenburg, F. and Davies, J.H. (1995). Slab breakoff: A model for syncollisional magmatism and tectonics in the Alps. *Tectonics*, 14(1), pp.120–131. doi:https://doi.org/10.1029/94tc02051.

Warr, L.N. (2021). IMA–CNMNC approved mineral symbols. *Mineralogical Magazine*, 85, pp.1–30. doi:https://doi.org/10.1180/mgm.2021.43.

Winter, J.D. (2014). *Principles of igneous metamorphic petrology*. Harlow: Pearson, Cop.

Yamato, P., Thibault Duretz and Angiboust, S. (2019). Brittle/Ductile Deformation of Eclogites: Insights From Numerical Models. *Geochemistry Geophysics Geosystems*, 20(7), pp.3116–3133. doi:https://doi.org/10.1029/2019gc008249.

14. Appendix

Figure 37: 1912a in PPL

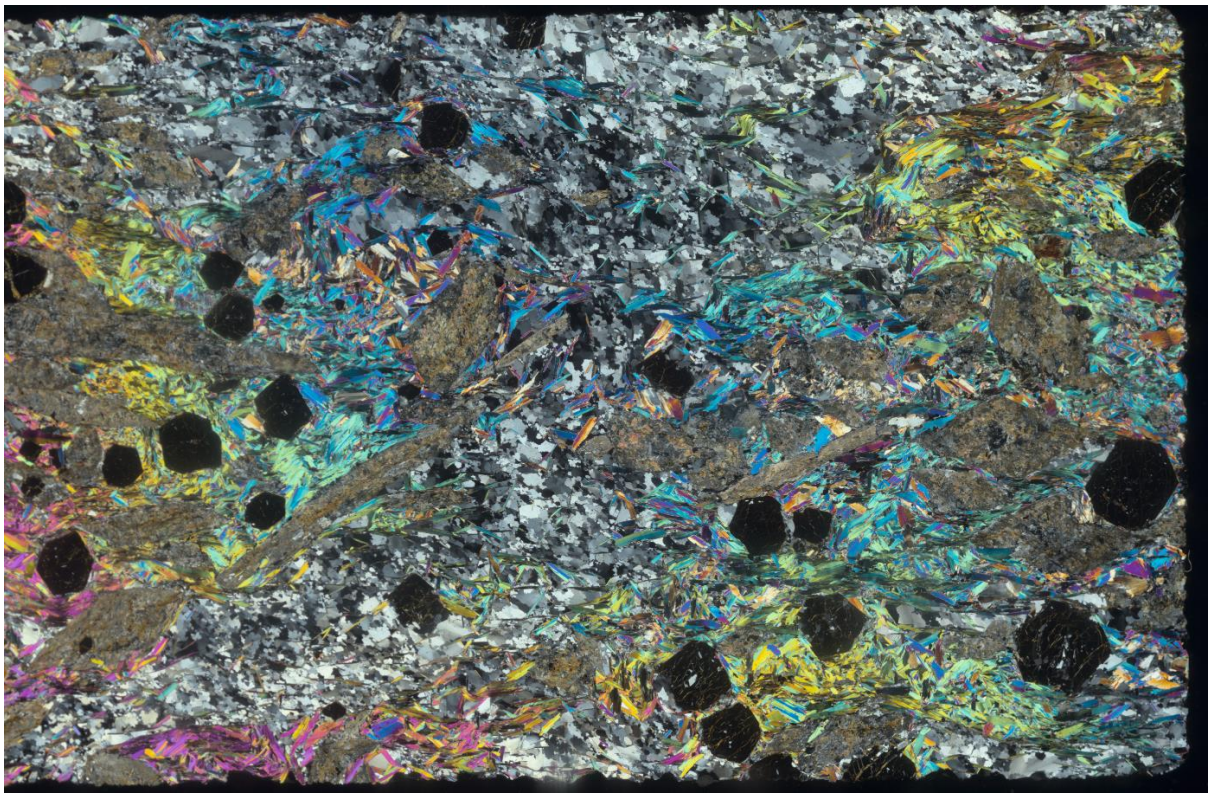

Figure 38: 1923a in XPL.

Figure 39: 1923b in PPL.

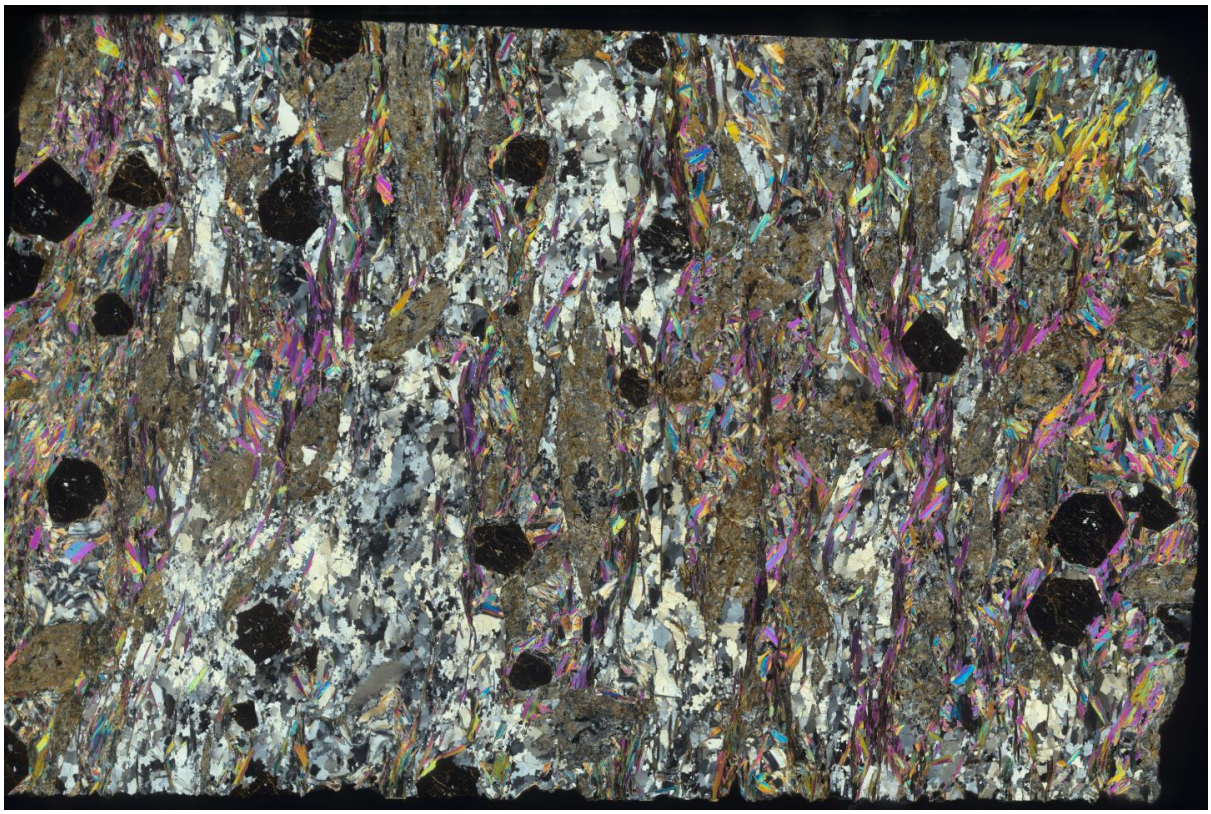

Figure 40: 1923b in XPL.

a.p.f.u.	Ctd Inclusion	Ctd Inclusion	Ctd Inclusion	Ctd Matrix	Ctd Matrix
Si	24.69	24.54	24.54	24.31	24.39
Ti	bdl	bdl	0.04	bdl	bdl
Cr	bdl	bdl	bdl	bdl	bdl
Al	41.04	40.59	41.01	40.73	40.93
Fe3+	23.39	24.34	24.45	23.12	24.38
Fe2+	0.03	0.19	0.17	0.03	0.23
Mn	bdl	bdl	0.04	bdl	0.03
Ni	3.38	2.59	2.53	3.81	2.56
Mg	0.02	0.03	bdl	0.01	bdl
Ca	bdl	0.01	bdl	bdl	0.01
Na	bdl	bdl	bdl	0.01	bdl
K	1.00	1.00	2.00	3.00	3.00
Oxide%					
SiO2	2.02	2.03	2.02	2.00	2.01
TiO2	0.00	0.00	0.00	0.00	0.00
Cr2O3	0.00	0.00	0.00	0.00	0.00
Al2O3	3.96	3.95	3.97	3.95	3.98
FeO	0.00	0.00	0.00	0.00	0.00
MnO	1.60	1.68	1.68	1.59	1.68
NiO	0.00	0.01	0.01	0.00	0.02
MgO	0.00	0.00	0.00	0.00	0.00
CaO	0.41	0.32	0.31	0.47	0.32
Na2O	0.00	0.00	0.00	0.00	0.00
K2O	0.00	0.00	0.00	0.00	0.00

Table 4: Selection of ctd chemical analyses. bdl = below detection limit.

a.p.f.u.	Chl Matrix	Chl Matrix	Chl Matrix	Chl Matrix	Chl Matrix	Chl Matrix
Si	2.71	2.71	2.71	2.69	2.71	2.74
Ti	0.01	0.01	0.01	0.01	0.01	0.00
Cr	0.00	0.00	0.00	0.00	0.00	0.00
Al	2.61	2.63	2.61	2.60	2.62	2.58
Fe3+	0.00	0.00	0.00	0.00	0.00	0.00
Fe2+	2.89	2.85	2.78	2.83	2.86	2.86
Mn	0.00	0.00	0.00	0.00	0.00	0.00
Ni	0.00	0.00	0.00	0.00	0.00	0.00
Mg	1.76	1.77	1.85	1.85	1.78	1.77
Ca	0.00	0.00	0.00	0.00	0.00	0.00
Na	0.00	0.00	0.01	0.02	0.00	0.01
K	0.00	0.00	0.00	0.00	0.00	0.00
Oxide%						
SiO2	24.79	24.82	25.03	24.66	24.77	25.26
Al2O3	20.28	20.44	20.47	20.20	20.27	20.20
FeO	31.71	31.28	30.71	31.05	31.31	31.60
CaO	0.01	0.02	0.02	0.02	0.00	0.00
TiO2	0.08	0.08	0.07	0.12	0.07	0.06
Na2O	0.00	0.02	0.05	0.10	0.00	0.04
MgO	10.84	10.86	11.43	11.38	10.90	10.97
P2O5	0.03	0.02	0.01	0.02	0.01	0.01
K2O	0.00	0.00	0.02	0.02	0.01	0.00
MnO	0.00	0.00	0.00	0.01	0.00	0.00
NiO	0.05	0.00	0.02	0.00	0.00	0.02
Cr2O3	0.01	0.00	0.06	0.00	0.00	0.00

Table 5: selection of chl chemical analyses. bdl = below detection limit.

a.p.f.u.	Mu in Grt	Mu in Grt	Mu in Grt	Mu Matrix	Mu Matrix
Si	3.28	3.35	3,28	3.55	3.56
Ti	0.01	0.01	0.01	0.01	0.01
Cr	0.00	0.00	0.00	0.00	0.00
Al	2.17	2.22	2.30	1.99	2.00
Fe3+	0.00	0.00	0.00	0.00	0.00
Fe2+	0.39	0.22	0.26	0.13	0.11
Mn	0.00	0.00	0.00	0.00	0.00
Ni	0.00	0.00	0.00	0.01	0.00
Mg	0.33	0.30	0.29	0.43	0.44
Ca	0.00	0.00	0.00	0.00	0.00
Na	0.05	0.05	0.06	0.02	0.01
K	0.85	0.81	0.76	0.67	0.62
SiO2	47.80	49.93	48.69	52.89	53.32
TiO2	0.22	0.20	0.23	0.15	0.13
Cr2O3	0.00	0.00	0.00	0.00	0.00
Al2O3	26.86	28.08	28.96	25.15	25.37
FeO	6.73	3.86	4.59	2.30	1.91
MnO	0.00	0.02	0.01	0.00	0.00
NiO	0.00	0.03	0.05	0.09	0.03
MgO	3.20	2.95	2.85	4.32	4.38
CaO	0.00	0.00	0.06	0.00	0.00
Na2O	0.37	0.39	0.45	0.15	0.11
K2O	9.67	9.41	8.79	7.89	7.31

Table 6: selection of mu chemical analyses. bdl = below detection limit.

a.p.f.u.	Alb	Alb	Bt	Bt	GAC	GAC	GAC	Mixed	Mixed
Si	2.96	2.97	2.72	2.54	----------	----------	----------	----------	----------
Ti	0.00	0.00	0.01	0.03	----------	----------	----------	----------	----------
Cr	0.00	0.00	0.00	0.00	----------	----------	----------	----------	----------
Al	1.03	0.96	1.82	1.80	----------	----------	----------	----------	----------
Fe3+	0.00	0.00	0.00	0.00	----------	----------	----------	----------	----------
Fe2+	0.01	0.09	1.28	1.52	----------	----------	----------	----------	----------
Mn	0.00	0.00	0.00	0.00	----------	----------	----------	----------	----------
Ni	0.00	0.00	0.00	0.01	----------	----------	----------	----------	----------
Mg	0.00	0.07	1.21	1.39	----------	----------	----------	----------	----------
Ca	0.03	0.03	0.01	0.00	----------	----------	----------	----------	----------
Na	0.97	0.80	0.01	0.01	----------	----------	----------	----------	----------
K	0.00	0.05	0.58	0.50	----------	----------	----------	----------	----------
SiO2	68.23	67.81	35.31	31.61	54.40	52.94	49.09	43.14	61.95
Al2O3	20.22	18.59	20.00	19.03	3.70	2.03	4.54	10.41	9.79
FeO	0.36	2.56	19.84	22.72	27.91	29.23	29.67	22.88	12.60
CaO	0.71	0.70	0.15	0.05	0.25	0.38	0.27	0.16	0.00
TiO2	0.03	0.02	0.20	0.43	0.00	0.04	0.11	0.03	0.02
Na2O	11.49	9.46	0.09	0.09	2.33	0.66	0.40	0.06	0.03
MgO	0.02	1.07	10.57	11.59	11.49	11.90	11.55	11.20	6.74
P2O5	0.02	0.00	0.04	0.02	0.00	0.09	0.18	0.07	0.02
K2O	0.03	0.87	5.86	4.87	0.01	0.14	0.60	2.36	5.61
MnO	0.00	0.00	0.00	0.00	0.04	0.01	0.00	0.00	0.00
NiO	0.02	0.01	0.05	0.11	0.04	0.04	0.03	0.00	0.03
Cr2O3	0.00	0.00	0.00	0.00	0.00	0.00	0.00	0.00	0.00
Closure	101.13	101.09	92.10	90.52	100.17	97.47	96.43	90.31	96.80

Table 7: Selection of mineral chemical analyses performed on glaucophane pseudomorphs. bdl = below detection limit.

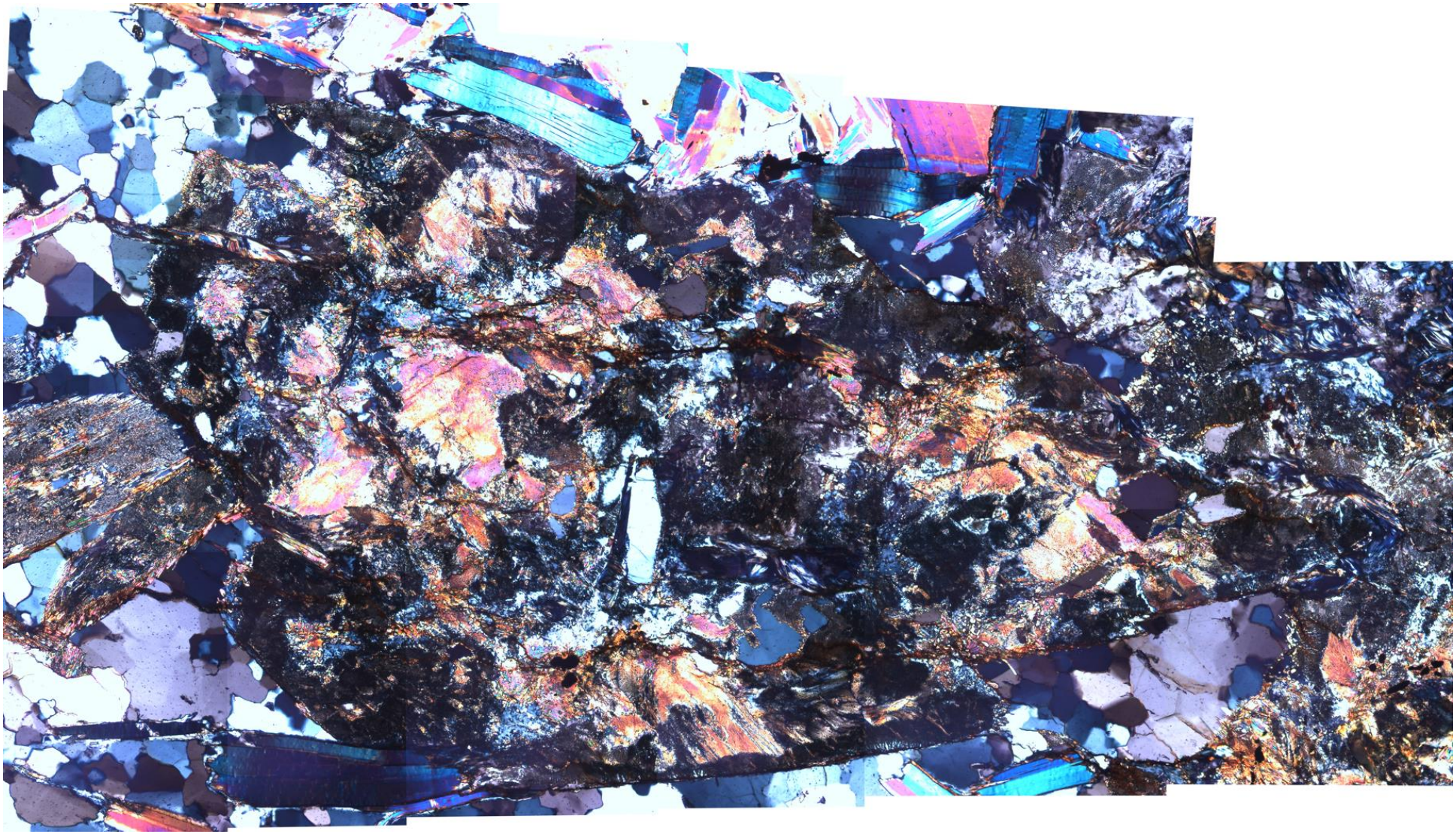

Figure 41: Glaucophane one multi-stitch available as supplementary material 1

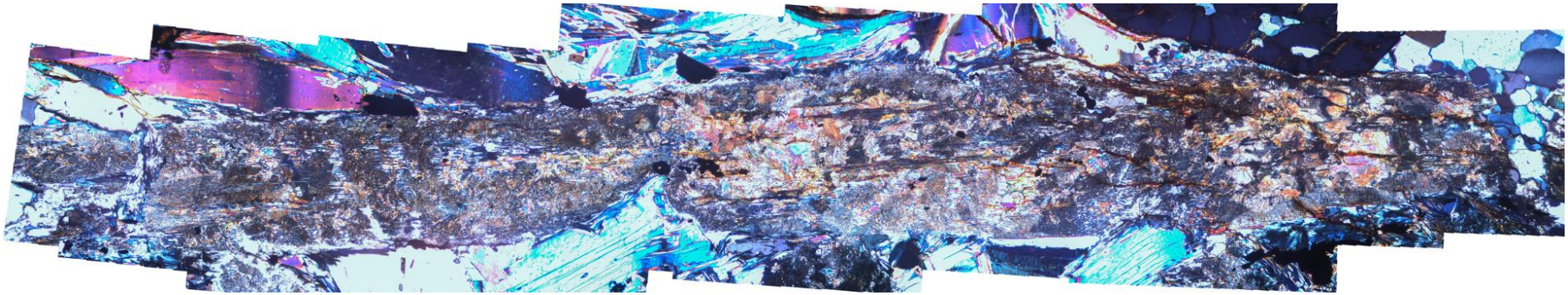

Figure 42: Glaucophane two multi-stitch, available as supplementary material 2

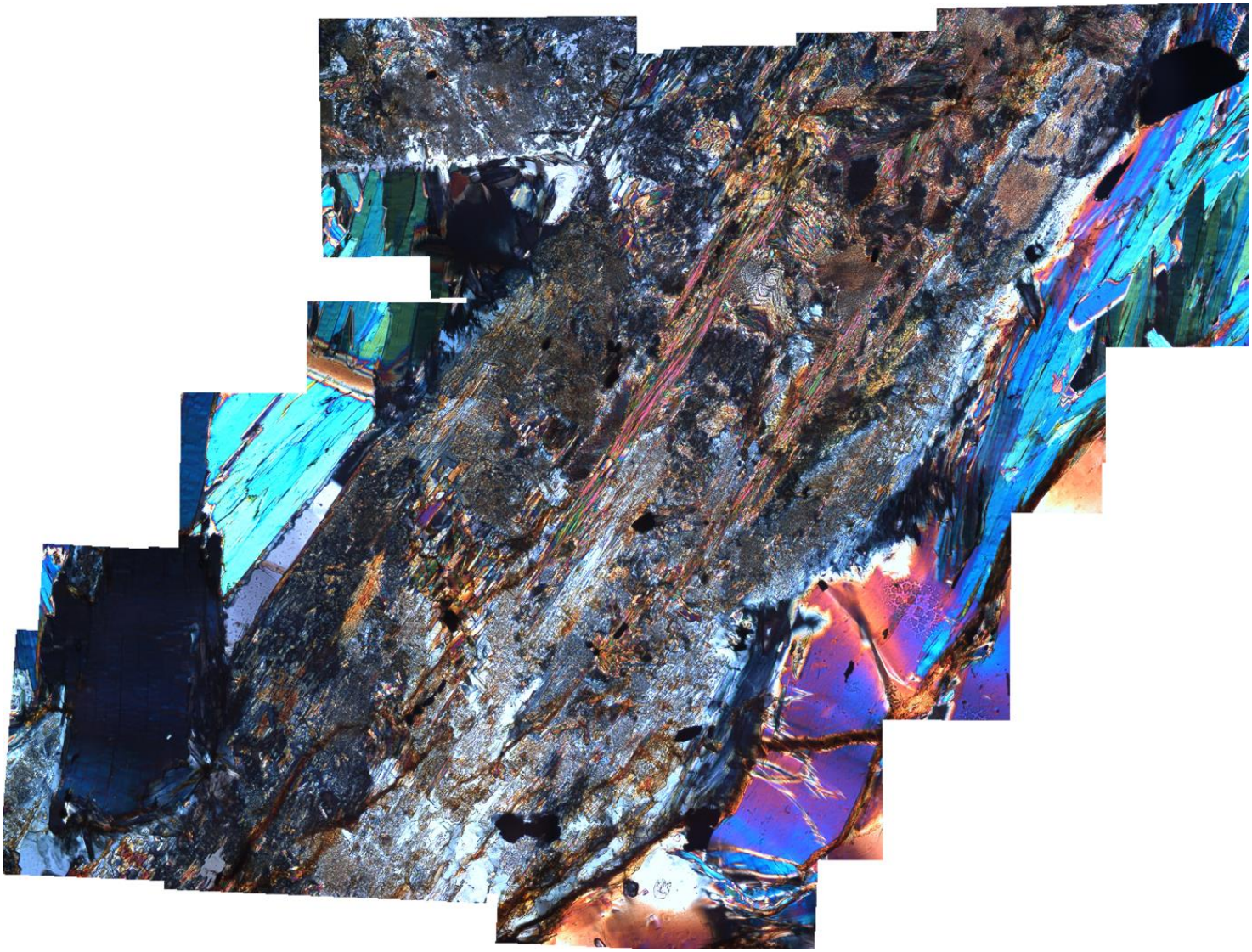

Figure 43: Glaucophane three multi-stitch, available as supplementary material 3